Università degli Studi di Padova

Dipartimento di Ingegneria Industriale DII

Corso di Laurea Magistrale in Ingegneria Aerospaziale

INVESTIGATION OF WAKE LOSS GENERATION IN THE WAKE OF A LINEAR LOW-PRESSURE TURBINE CASCADE USING RANS AND LES METHODS

Relatore: Prof. Federico Dalla Barba

Laureando: PIETRO ARDENTI
Matricola: 2056129

"Considerate la vostra semenza:
fatti non foste a viver come bruti,
ma per seguir virtute e canoscenza."

— Dante Alighieri, Inferno XXVI

Abstract

Motivated by ambitious efficiency and emissions targets, the future of aircraft design necessitates significant changes. These changes will impact the role and design of aero-engines, demanding higher fidelity and coupled modeling approaches. Scale-resolving simulations (SRS) are gaining traction in turbomachinery design, but their computational cost remains a major hurdle. Therefore, Reynolds-averaged Navier-Stokes (RANS) simulations remain the industry standard for performance evaluation in components like low-pressure turbines. This research investigates the limitations of RANS models in predicting loss generation compared to Large Eddy Simulations (LES). Within this study, multiple simulations were conducted using the DLR's TRACE flow solver for two distinct setups and operating points, ($\text{Re} = 90\,000$ and $\text{Re} = 200\,000$). RANS closure models (SST k-ω and SSG/LRR-ω) representing Linear Eddy-Viscosity Models (LEVMs) and Reynolds Stress Models (RSMs) were employed. Results were compared to pre-existing LES simulations and experimental data. The validation process confirmed the shortcomings of RANS simulations in capturing the fluid dynamics within the separation zone and wake for both operating points. A comprehensive analysis of entropy loss generation was conducted to assess system efficiency. This involved decomposing the total loss into individual terms associated with different loss mechanisms, allowing for understanding their contributions and spatial distribution. Both RANS turbulence models exhibited limitations compared to Large Eddy Simulations (LES) in accurately predicting losses when applied to flows involving separation and transition. While using LES data for inlet boundary conditions demonstrably improved simulation accuracy, it also highlighted the limitations of RANS methods in capturing Reynolds stresses and other turbulence quantities.

Sommario

Nel contesto di ambiziosi obiettivi di efficientamento e riduzione delle emissioni, il panorama della progettazione aeronautica si avvia verso un futuro di sostanziali cambiamenti. Tali innovazioni influenzeranno il ruolo e la progettazione dei motori aeronautici, richiedendo l'implementazione di approcci di modellazione di elevata accuratezza. Le simulazioni con risoluzione di scala (SRS) stanno acquisendo sempre maggiore rilevanza nel campo della progettazione di turbomacchine, sebbene il loro costo computazionale rappresenti ancora un ostacolo significativo. Pertanto, le simulazioni basate sulle equazioni di Navier-Stokes mediate alla Reynolds (RANS) rimangono lo standard industriale per la valutazione delle prestazioni in componenti quali le turbine a bassa pressione. Il presente studio si propone di investigare i limiti intrinseci dei modelli RANS nella predizione della generazione di perdite rispetto alle simulazioni Large Eddy Simulations (LES). A tal fine, sono state condotte molteplici simulazioni avvalendosi del risolutore di flusso TRACE del DLR per due distinte configurazioni e altrettanti punti operativi ($Re = 90\,000$ e $Re = 200\,000$). L'analisi ha coinvolto l'utilizzo di due modelli di chiusura RANS, vale a dire SST k-ω e SSG/LRR-ω, rappresentanti rispettivamente Linear Eddy-Viscosity Models (LEVMs) e Reynolds Stress Models (RSMs). I risultati ottenuti sono stati quindi confrontati con simulazioni LES preesistenti e dati sperimentali. Il processo di convalida ha confermato le carenze delle simulazioni RANS nel catturare correttamente la dinamica del fluido all'interno della zona di separazione e della scia per entrambi i regimi di funzionamento considerati. Successivamente, è stata condotta un'analisi approfondita della generazione di perdite di entropia al fine di valutare l'efficienza del sistema. Tale analisi ha comportato la scomposizione della perdita totale in termini di contributi individuali associati ai diversi meccanismi di perdita, consentendo di comprenderne l'entità e la distribuzione spaziale. Entrambi i modelli di turbolenza RANS hanno evidenziato delle limitazioni rispetto alle simulazioni LES nel prevedere con accuratezza le perdite in presenza di flussi che coinvolgono fenomeni di separazione e transizione. L'utilizzo di dati LES per le condizioni al contorno in ingresso ha indubbiamente migliorato la precisione della simulazione, pur evidenziando ulteriormente le limitazioni dei metodi RANS nel catturare gli sforzi di Reynolds e altre grandezze di turbolenza.

Contents

Contents

List of Figures

List of Tables

List of Symbols

Symbol	Description	Unit
ρ	Density	kg/m^3
t	Time	s
$\boldsymbol{u}$	Velocity vector	m/s
p	Pressure	Pa
$\boldsymbol{I}$	Identity tensor	m/s
$\boldsymbol{\tau}$	Viscous stress tensor	m/s^2
$\boldsymbol{f_e}$	External volume forces per unit mass	N/kg
E	Specific total energy	J/kg
e	Specific internal energy	J/kg
H	Specific total enthalpy	J/kg
h	Specific enthalpy	J/kg
T	Temperature	K
k_t	Thermal conductivity coefficient	W/(m K)
W_f	Work of external volume forces	kg m/s^3
Q	Heat production rate per unit volume	kg m/s^3
μ	Dynamic viscosity	Pa s
u_i, u_j, u_k	Velocity components	m/s
λ	Volumetric viscosity	Pa s
δ_{ij}	Kronecker delta	[-]
ν	Kinematic viscosity	m^2/s
R	Specific gas constant	J/(kg K)
c_p	Isobaric specific heat capacity	J/(kg K)
c_v	Isochoric specific heat capacity	J/(kg K)
μ_0	Reference viscosity	Pa s
T_0	Reference temperature	K
S_0	Sutherland constant	K
γ	Specific heats ratio	[-]
Pr	Prandtl number	[-]
Re	Reynolds number	[-]
L	Characteristic length	m
A	Generic flow variable	
τ_{ij}^v	Viscous stresses	m/s^2
τ_{ij}^R	Reynolds stresses	m/s^2
k	Turbulent kinetic energy	m^2/s^2
$\boldsymbol{F_D}$	Heat diffusive flux	W/m^2
$\boldsymbol{F_D^T}$	Total turbulent heat flux	W/m^2
ν_T	Turbulence eddy viscosity	m^2/s
σ_k	Turbulent Prandtl number	[-]
ε	Turbulence dissipation rate	J/(kg s)
ω	Specific turbulence dissipation rate	1/s

P_k	TKE rate of production	J/kg
S_{ij}	Strain rate tensor	1/s
C_{ij}	Convection term	$\mathrm{kg\,s^2/m}$
$D_{T,ij}$	Turbulent diffusion term	$\mathrm{kg\,s^2/m}$
$D_{L,ij}$	Molecular diffusion term	$\mathrm{kg\,s^2/m}$
P_{ij}	Stress production term	$\mathrm{kg\,s^2/m}$
ϕ_{ij}	Pressure strain term	$\mathrm{kg\,s^2/m}$
ε_{ij}	Dissipation term	$\mathrm{kg\,s^2/m}$
F_{ij}	Production by system rotation term	$\mathrm{kg\,s^2/m}$
R_{ij}	Reynolds stress tensor (for SSG/LRR-ω)	$\mathrm{m/s^2}$
b_{ij}	Anisotropy tensor	[-]
S_{ij}^*	Traceless strain rate tensor	1/s
$\widetilde{\Omega}_{ij}$	Rotational tensor (for RANS)	1/s
$G_\Delta(\boldsymbol{r})$	LES filter kernel	
Δ	Filter length scale	
a_{ij}	Reynolds stress tensor (for LES)	$\mathrm{m/s^2}$
τ_{ij}	Subgrid scale stress tensor (for LES)	$\mathrm{m/s^2}$
V	Cell volume	$\mathrm{m^3}$
$\bar{\Omega}_{ij}$	Rotational tensor (for LES)	1/s
S_{ij}^d	WALE tensor	$\mathrm{1/s^2}$
δ	Boundary layer thickness	m
τ_w	Wall shear stress	Pa
S	Total entropy	J/K
$\dot{S}$	Entropy rate of change	$\mathrm{J/(K\,s)}$
I_S	Entropy current	$\mathrm{J/(K\,s)}$
G_S	Entropy generation rate	$\mathrm{kg/(m\,K\,s^3)}$
G_s^{TOT}	Overall entropy generation rate	$\mathrm{kg/(m\,K\,s^3)}$
s	Specific entropy	$\mathrm{J/(K\,kg)}$
F_i	Entropy flux	$\mathrm{kg/(m^2\,K\,s^3)}$
q_j^R	Turbulent heat flux	$\mathrm{kg\,K/(m^2\,s)}$
V_M	Mean viscous dissipation term	$\mathrm{kg/(m\,K\,s^3)}$
H_M	Mean flow heat flux term	$\mathrm{kg/(m\,K\,s^3)}$
P_R	Turbulent production term	$\mathrm{kg/(m\,K\,s^3)}$
H_R	Turbulent heat flux term	$\mathrm{kg/(m\,K\,s^3)}$
A_k	TKE advection term	$\mathrm{kg/(m\,K\,s^3)}$
V_S	SGS stress dissipation term	$\mathrm{kg/(m\,K\,s^3)}$
H_S	SGS heat flux term	$\mathrm{kg/(m\,K\,s^3)}$
q_j^{SGS}	SGS turbulent heat flux	$\mathrm{kg\,K/(m^2\,s)}$
τ_{ij}^{SGS}	SGS stress tensor	$\mathrm{m/s^2}$
Ma	Mach number	[-]
Ma_{is}	Isentropic Mach number	[-]
ω	Total pressure loss coefficient (in Results)	[-]
c_{ax}	Axial chord	m
$\bar{\cdot}$	Time-averaged (in RANS)	
$\tilde{\cdot}$	Favre-averaged	
$\cdot'$	Fluctuating part	
$\cdot''$	Favre-averaged fluctuating part	

$\bar{\cdot}$ Filtered part (in LES)

$\cdot'$ Sub-filter part (in LES)

Indices

∞	Free-stream flow quantity
0	Reference value
1	Inlet position
2	Outlet position

Abbreviations

CFD	Computational Fluid Dynamics
IST	Institut für Strahlantriebe und Turbomaschinen
DLR	Deutsches Zentrum für Luft- und Raumfahrt
MTU	Motoren- und Turbinen-Union (MTU Aero Engines Holding AG)
ASME	The American Society of Mechanical Engineers
LPT	Low Pressure Turbine
LES	Large Eddy Simulation
DNS	Direct Numerical Simulation
RANS	Reynolds-Averaged Navier-Stokes Equations
LEVM	Linear Eddy Viscosity Model
NLEVM	Nonlinear Eddy Viscosity Model
RSM	Reynolds Stress Model
SST	Shear Stress Transport
SSG/LRR	Speziale-Sarkar-Gatski/Launder-Reece-Rodi
BSL	Baseline
SGS	Subgrid-Scale
TRACE	Turbomachinery Research Aerodynamic Computational Environment
TKE	Turbulent Kinetic Energy
L.E.	Leading Edge
T.E.	Trailing Edge
STG	Synthetic Turbulence Generator
GTF	Geared Turbofan

1. Introduction

Within this chapter, the initial section introduces the motivation behind the undertaking of the current work. Following this, an overview of the objectives and the structure of the thesis is presented.

1.1. Motivation

The relentless push towards sustainable air travel hinges on advancements in key areas: efficiency, noise reduction, and overall environmental impact. While progress has been made, further breakthroughs are key to achieve ambitious environmental goals. In this context, the crucial low-pressure turbine (LPT) holds immense potential for driving the future of aeronautics. Modern LPTs are responsible for up to $30\,\%$ of the engine weight and supplies power to the fan section, generating as much as $80\,\%$ of the engine thrust [17]. A recent innovation in fuel efficiency is the geared turbofan (GTF) engine. This technology incorporates a planetary reduction gearbox positioned between the fan and the low-pressure (LP) shaft. By decoupling their rotational speeds, GTF engines allow the LP shaft to operate at a higher speed, enabling a reduction in the number of stages required in both the LP compressor and turbine. This configuration translates to increased efficiency and weight reduction. Furthermore, GTF engines facilitate the implementation of lower fan speeds and higher bypass ratios, which directly contribute to diminished fuel consumption and significantly decreased noise emissions. Another LPT design strategy is to reduce the engine's weight by reducing the number of blades and increasing the blade loading thereby. In doing this, the flow is forced to turn more aggressively around the blade, resulting in thicker boundary layers and increased frictional losses. Moreover, due to strong adverse pressure gradients, the pressure on the suction side of the blade decreases and can lead to flow separation, where the flow detaches from the blade surface and creates turbulence. Separation significantly reduces lift generation and further increases losses. This problem is exacerbated by the Reynolds number range for various operating conditions. The Reynolds numbers of LPT blades varies from about 0.5×10^5 in the final stage at high altitude to about 5×10^5 at sea level takeoff in the first stage of the largest turbofans. Between takeoff and cruise altitude, the Reynolds number might fall by a factor of between 3 and 4. For these low values of Reynolds number ($<1 \times 10^5$), LPT blades exhibit large separation bubbles on their suction sides. This can lead to an increase in profile losses up to $300\,\%$ compared to their design point [23]. In order to maximize the blade loading and to avoid a non-reattachment of the separation bubble, it is crucial that numerical design tools are sufficiently accurate to predict the correct reattachment.

Investigating LPTs behaviour and predicting the development of losses is responsibility of Computational Fluid Dynamics (CFD). In the field of science, more and more researchers are striving for three-dimensional scale-resolving simulations, such as Large-Eddy

Simulation (LES), and Direct Numerical Simulation (DNS). These methods offer the temporal and spatial prediction of turbulent scales, up to primary instability mechanisms in boundary layers, but are much more resource intensive. Only in the recent years, with increasing availability of computational resources and advancement in high-order discretization, these techniques are getting used more widely. For this reason, even today the most utilized tool are Reynolds-averaged Navier-Stokes (RANS) methods, which are still the only cost-efficient simulations. Compared to the aforementioned methods, RANS offer a significant advantage in computational cost. This renders them particularly suitable for preliminary design stages and optimization studies, where numerous simulations are necessary to explore the design space effectively. They can still provide reasonably accurate predictions for average flow quantities like pressure, temperature, and velocity in LPTs. This information is often sufficient for initial design stages when the focus is on overall performance trends and gross design features. Furthermore, over the years, a well-established workflow and extensive toolset have been developed around RANS methods for LPT simulations. This means engineers have extensive experience using these tools and can interpret the results with a good level of understanding. However, being based on temporal averaging and modeling of transition and turbulence, they still lack prediction accuracy, especially the closer the test case is to the physical limitations in terms of weak transitional boundary layers, the decay of turbulence, complex turbulent structures, or intensive flow separation [8].

As highlighted earlier, the flow conditions within low-pressure turbines frequently exhibit these phenomena, making accurate prediction of the separation bubble on the suction side crucial for downstream wake characterization. This region holds significant interest as it contributes substantially to overall losses. Previous studies have documented the limitations of Reynolds-averaged Navier-Stokes (RANS) simulations in accurately capturing Reynolds stresses, leading to underestimation of wake thickness and overestimation of peak losses. Denton [7] provided a comprehensive overview of loss origins and effects in turbomachines. Recent years have witnessed increased research efforts focused on assessing and quantifying these losses through various methods. Bear et al. [1] employed stereoscopic particle image velocimetry (PIV) data and total pressure loss data to explore the mechanisms of loss production within an LPT cascade, focusing on the description of the secondary flow field. Lengani et al. [22] utilized PIV measurements in conjunction with proper orthogonal decomposition (POD) to identify and assess the sources of turbulence kinetic energy (TKE) production within LPT cascades. Wheeler et al. [44] investigated the influence of turbulence on both surface flow physics and heat transfer within LPT vanes. Their work also included an analysis of loss development through the vane passage. Among various quantities employed to quantify the efficiency of components in turbomachines, entropy has gained widespread acceptance, as evidenced by Bejan [2]. For the scope of this research, a similar approach to the one employed by Zhao and Sandberg [46] will be followed; after deriving the entropy transport equations based on averaged flow quantities, the entropy generation process is fully decomposed into individual terms representing distinct physical mechanisms. These terms will then be employed to quantify the RANS modeling error associated with turbulence closure models and to locate the major error source within the vane, subsequently enabling a comparison with the results obtained from LES simulations of the same geometry.

1.2. Objectives and Outline of the Present Work

While scale-resolving simulations are increasingly employed in the design process of turbomachines, their significant computational costs continue to present a challenge. Consequently, RANS simulations remain the industry standard for performance evaluations in components like low-pressure turbines. This research aims to identify the limitations of RANS models in predicting loss generation compared to LES, providing valuable insights for refining RANS approaches and improving their accuracy in the context of industrial applications.

The thesis is structured as follows. Chapter 2 introduces the theoretical background of CFD simulations, including the governing equations. It then discusses RANS and LES computational methods, focusing on the two turbulence models used for RANS simulations. Additionally, the chapter provides a brief overview of the characteristics of wake flows and presents the theory behind entropy loss generation mechanisms. Chapter 3 introduces the main features of the investigated geometry, the MTU-T161 low-pressure turbine (LPT). It then details the different simulation setups used and summarizes the software utilized throughout the research. Chapter 4, presents the validation process using experimental data and analyzes the results using the entropy generation approach. It compares results obtained from RANS and LES simulations for the first operating point, analyzing various setups. Additionally, the chapter compares RANS data for the two investigated operating points. Finally, Chapter 5 draws conclusions based on the research findings and provides a perspective on future research directions. Further, the grid independence study is described in Appendix A.

2. Fundamentals of Compressible Fluids

In this chapter, an overview on computational methods is provided, starting with the flow governing equations and continuing with the analysis of the closure problem and turbulence modeling. In the end a brief summary on wake flows and entropy generation losses is given.

2.1. Fluid Governing Equations

2.1.1. Navier-Stokes Equations

The Navier-Stokes equations are a set of partial differential equations which describes the motion of viscous fluids, named after french engineer and physicist Claude-Louis Navier and Anglo-Irish physicist and mathematician George Gabriel Stokes. The Navier-Stokes equations mathematically express the conservation of momentum and the conservation of mass for Newtonian fluids. For a compressible fluid, the Navier-Stokes equations (mass and momentum conservation) can be expressed together with the equation for the conservation of energy in the so-called conservation form as:

$$\frac{\partial \rho}{\partial t} + \nabla \cdot (\rho \boldsymbol{u}) = 0, \tag{2.1}$$

$$\frac{\partial (\rho \boldsymbol{u})}{\partial t} + \nabla \cdot (\rho \boldsymbol{u} \otimes \boldsymbol{u}) = -\nabla \cdot (p\boldsymbol{I}) + \nabla \cdot \boldsymbol{\tau} + \rho \boldsymbol{f_e}, \tag{2.2}$$

$$\frac{\partial (\rho E)}{\partial t} + \nabla \cdot (\rho \boldsymbol{u} H) = \nabla \cdot (\boldsymbol{\tau} \cdot \boldsymbol{u}) + \nabla \cdot (k_t \nabla T) + W_f + Q, \tag{2.3}$$

where ρ is the density, $\boldsymbol{u} = (u,v,w)$ the velocity, p the pressure, $\boldsymbol{I}$ the unit tensor, T the temperature, k_t the thermal conductivity coefficient, $\boldsymbol{f_e}$ external volume forces per unit mass and Q is the rate per unit volume of internal heat production. The variable E is the specific total energy and is given by the sum of the specific kinetic energy and specific internal energy, respectively:

$$E = \frac{1}{2} \boldsymbol{u} \cdot \boldsymbol{u} + e. \tag{2.4}$$

The quantity W_f is the work of the external volume forces and is defined as:

$$W_f = \rho \boldsymbol{f_e} \cdot \boldsymbol{u}. \tag{2.5}$$

It is also useful to define the enthalpy of the fluid as $h = e + p/\rho$ from which we can derive the stagnation or total enthalpy H:

$$H = e + \frac{p}{\rho} + \frac{1}{2}\boldsymbol{u} \cdot \boldsymbol{u} = h + \frac{1}{2}\boldsymbol{u} \cdot \boldsymbol{u} = E + p/\rho. \tag{2.6}$$

The tensor $\boldsymbol{\tau}$ is the viscous shear stress tensor that can be expressed in indexing notation as:

$$\tau_{ij} = \left[\mu\left(\frac{\partial u_j}{\partial x_i} + \frac{\partial u_i}{\partial x_j}\right) + \lambda\left(\frac{\partial u_k}{\partial x_k}\right)\delta_{ij}\right], \tag{2.7}$$

where μ is the dynamic viscosity, λ the volumetric viscosity and δ_{ij} the Kronecker delta. It is possible to define a kinematic viscosity in the following form:

$$\nu = \frac{\mu}{\rho}. \tag{2.8}$$

Using the Stokes assumption the volumetric viscosity can be expressed as:

$$\lambda = -\frac{2}{3}\mu, \tag{2.9}$$

so the viscous shear stress tensor can be recast as:

$$\tau_{ij} = \mu\left[\left(\frac{\partial u_j}{\partial x_i} + \frac{\partial u_i}{\partial x_j}\right) - \frac{2}{3}\left(\frac{\partial u_k}{\partial x_k}\right)\delta_{ij}\right]. \tag{2.10}$$

These equations are valid for Newtonian fluids, which are fluids that exhibit a linear relationship between shear stress and shear rate. In other words, the viscosity of the fluid remains constant under varying shear conditions.

As of now, the Navier-Stokes system of equations contains 5 equations and 7 unknowns, u, v, w, p, T, ρ and e. The closure of the systems is possible by employing state equations for pressure, temperature, density and internal energy. For an ideal gas we have:

$$\begin{aligned} p &= \rho RT, \\ e &= c_v T, \end{aligned} \tag{2.11}$$

with $R = 287.06 \, \frac{\text{J}}{\text{kg K}}$ the specific gas constant and c_v the isochoric specific heat capacity.

It is even possible to define the dynamic viscosity as for the Sutherland's law:

$$\mu = \mu_0 \frac{T_0 + S_0}{T + S_0} \left(\frac{T}{T_0}\right)^{\frac{3}{2}}, \tag{2.12}$$

considering the reference viscosity $\mu_0 = 1.7198 \times 10^{-5} \frac{\text{kg}}{\text{m s}}$ at the reference temperature $T_0 = 273 \, \text{K}$ and the Sutherland constant $S_0 = 110 \, \text{K}$.

For this research, air is used as working fluid, assumed as an ideal gas, with a constant ratio of specific heats $\gamma = c_p/c_v = 1.4$ and Prandtl number $Pr = 0.72$.

Another relevant number for the matter of this study is the Reynolds number, a dimensionless quantity representing the ratio of inertial forces to viscous forces within a fluid that is subjected to relative internal movement due to different fluid velocities:

$$Re = \frac{uL}{\nu} = \frac{\rho u L}{\mu}, \tag{2.13}$$

where all quantities are the same already mentioned except for L which is the characteristic length, i.e. a dimension that defines the scale of the physical system. From the value of the Reynolds number it is possible to distinguish between laminar (low Re) and turbulent flow (high Re), with the former where viscous forces are dominant, and is characterized by smooth, constant fluid motion while the latter is dominated by inertial forces, which tend to produce chaotic eddies, vortices and other flow instabilities.

2.1.2. RANS: Reynolds (Favre)-Averaged Navier-Stokes Equations

Due to their nature of non-linear partial differential equations, it is impossible to solve analytically the Navier-Stokes equations as they are. Even for simple problems, assumptions and approximations are necessary to simplify the equations in order to derive an analytical solution. Thus, especially when analyzing complex, turbulent systems, a different way from analytical solution is needed and in the past, scientists have come up with a solution in the form of averaging the equations.

The Reynolds-averaged Navier-Stokes equations are derived by averaging the viscous conservation laws over a time interval T, that must be large compared to the typical time scale of the fluctuations; if T is large enough, A does not depend on the time at which the averaging is started. For any flow variable A it is possible to define a turbulent fluctuating part A' so that:

$$A = \bar{A} + A', \tag{2.14}$$

where

$$\bar{A}(\boldsymbol{x}, t) = \frac{1}{T} \int_{-T/2}^{T/2} A(\boldsymbol{x}, t + \tau) \mathrm{d}\tau, \tag{2.15}$$

is the time-averaged turbulent quantity.

For compressible flows, the averaging process leads to products of fluctuations between density and other variables such as velocity or internal energy. In order to avoid their explicit occurrence, a density-weighted average, also known as Favre-averaging can be introduced:

$$\widetilde{A} = \frac{\overline{\rho A}}{\bar{\rho}}, \tag{2.16}$$

with

$$A = \widetilde{A} + A'', \tag{2.17}$$

and

$$\overline{\rho A''} = 0. \tag{2.18}$$

This way of defining mean turbulent variables will remove all extra products of density fluctuations with other fluctuating quantities. The averaged continuity equation becomes:

$$\frac{\partial}{\partial t} \bar{\rho} + \nabla \cdot (\bar{\rho} \widetilde{\boldsymbol{u}}) = 0. \tag{2.19}$$

As for the averaged momentum equations we get:

$$\frac{\partial \bar{\rho} \widetilde{\boldsymbol{u}}}{\partial t} + \nabla \cdot (\bar{\rho} \widetilde{\boldsymbol{u}} \otimes \widetilde{\boldsymbol{u}}) = -\nabla \cdot \bar{p} \boldsymbol{I} - \nabla \cdot (\widetilde{\boldsymbol{\tau}}^{\mathrm{v}} - \boldsymbol{\tau}^R) + \rho \boldsymbol{f_e}, \tag{2.20}$$

where the Reynolds stresses $\boldsymbol{\tau}^{\mathrm{R}}$ defined by

$$\boldsymbol{\tau}^{\mathrm{R}} = -\overline{\rho \boldsymbol{u}'' \otimes \boldsymbol{u}''}, \tag{2.21}$$

are added to the averaged viscous shear stresses $\widetilde{\boldsymbol{\tau}}^{\mathrm{v}}$. In Cartesian coordinates we have:

$$\boldsymbol{\tau}_{ij}^{\mathrm{R}} = -\overline{\rho u_i'' u_j''}. \tag{2.22}$$

It is to be observed that all the effects of the turbulence on the averaged momentum conservation are contained in the Reynolds stress term.

The derivation of the turbulent-averaged energy conservation equation is more complex, since a distinction has to be made between the averaged total energy $\widetilde{E}$ and the total energy of the averaged flow $\hat{E}$. These two quantities differ by the kinetic energy of the turbulent fluctuations. If we define the mean turbulent total energy by the straightforward relation, the over-bar indicating the time average:

$$\bar{\rho}\widetilde{E} = \overline{\rho E} = \overline{\rho(e + \frac{\boldsymbol{u}}{2})}, \tag{2.23}$$

we obtain:

$$\widetilde{E} = \widetilde{e} + \widetilde{k} + k \equiv \hat{E} + k, \tag{2.24}$$

where $\widetilde{k}$ is the kinetic energy of the mean flow per unit mass,

$$\bar{\rho}\widetilde{k} = \bar{\rho}\frac{\widetilde{\boldsymbol{u}}^2}{2}, \tag{2.25}$$

and k is the turbulent kinetic energy; thus:

$$\bar{\rho}k = \overline{\rho\frac{\boldsymbol{u}'^2}{2}} \equiv \overline{\rho k''}, \tag{2.26}$$

is defined as the average of the kinetic energy k'' of the turbulent fluctuations. Similarly the averaged total enthalpy is defined by:

$$\widetilde{H} = \widetilde{E} + \frac{\bar{p}}{\bar{\rho}} = \widetilde{h} + \widetilde{k} + k \equiv \hat{H} + k, \tag{2.27}$$

where $\hat{H}$ is the stagnation enthalpy of the averaged flow.

The fluctuating components are given by:

$$H'' = h'' + \boldsymbol{u}'' \cdot \widetilde{\boldsymbol{u}} + k'' - k \tag{2.28}$$

$$E'' = e'' + \boldsymbol{u}'' \cdot \tilde{\boldsymbol{u}} + k'' - k. \tag{2.29}$$

A conservative form of the turbulent energy equation is obtained by averaging the energy conservation equation, in the absence of external sources, leading to:

$$\frac{\partial}{\partial t}(\bar{\rho}\hat{E}) + \nabla \cdot (\bar{\rho}\hat{H}\boldsymbol{u}) = \nabla \cdot (-\overline{\boldsymbol{F}_D} + \overline{\boldsymbol{u} \cdot \boldsymbol{\tau}^T} - \overline{\rho h'' \boldsymbol{u}''}), \tag{2.30}$$

where the heat diffusive flux is $\boldsymbol{F_D} = -(\mu c_p/Pr)\overline{\nabla T}$. The influence of the turbulent fluctuations on the energy balance of the time-averaged flow is expressed by a turbulent heat flux vector, equal to $(-\overline{\rho H'' \boldsymbol{u}''})$. In the above equation the total shear stress tensor $\overline{\boldsymbol{\tau}}^{\mathrm{T}}$ is defined by

$$\boldsymbol{\tau}^{\mathrm{T}} = \boldsymbol{\tau}^{\mathrm{v}} + \boldsymbol{\tau}^R, \tag{2.31}$$

as the sum of the averaged viscous stresses $\overline{\boldsymbol{\tau}}^{\mathrm{v}}$ and the Reynolds stresses $\boldsymbol{\tau}^{\mathrm{R}}$.

Similarly we can define a total turbulent heat flux term as:

$$\boldsymbol{F_D^T} = -\frac{\mu c_p}{Pr}\overline{\nabla T} + \overline{\rho h'' \boldsymbol{u}''}. \tag{2.32}$$

2.2. Turbulence Models

Unfortunately the equations averaging procedure has generated both the Reynolds stresses and the turbulent heat flux terms, which now pose a new problems as there are more unknowns than equations. This is called the closure problem and the only way to solve it is through developing turbulence models that are needed, in fact, to model these unknown quantities. There are various closure models developed to approximate the Reynolds stresses and their choice can significantly impact the accuracy of RANS predictions for turbulent flows. There are three major classes into which the models can be divided:

- Linear Eddy Viscosity Models (LEVM): the Reynolds stresses are modelled by a linear constitutive relationship with the mean flow straining field;

- Nonlinear Eddy Viscosity Models (NLEVM): an eddy viscosity coefficient is used to relate the mean turbulence field to the mean velocity field, however in a nonlinear relationship;

- Reynolds Stress Models (RSM): unlike eddy viscosity models, RSMs directly solve transport equations for individual Reynolds stresses, providing a more detailed representation of turbulence. However, RSMs are computationally more expensive.

In this section we are going to analyze only the models which are relevant for our research, in particular the Menter SST model which is part of the LEVMs and the SSG/LRR-ω model which is included into RSMs.

2.2.1. LEVMs and Menter SST k-ω Model

One of the most significant contributions to turbulence modelling was presented in 1877 by Boussinesq [4]. His idea is based on the observation that the momentum transfer in a turbulent flow is dominated by the mixing caused by large energetic turbulent eddies. The Boussinesq hypothesis assumes that the turbulent shear stress depends linearly on the mean rate of strain, as in a laminar flow. The proportionality factor is the turbulence eddy viscosity $\nu_T > 0$. For computational simplicity, the eddy viscosity, is often computed in terms of a mixing length, that is analogous to the mean free path in a gas. In contrast to the molecular viscosity, which is an intrinsic property of the fluid, the eddy viscosity (and hence the mixing length) depends upon the flow. Because of this, the eddy viscosity and mixing length must be specified in advance, most simply, by an algebraic relation between eddy viscosity and length scales of the mean flow. This way we can write the Reynolds stresses as:

$$-\rho\overline{u_i'u_j'} = \nu_T(\frac{\partial \bar{u}_i}{\partial x_j} + \frac{\partial \bar{u}_j}{\partial x_i}) - \frac{2}{3}\rho\delta_{ij}k, \tag{2.33}$$

with k, the turbulent kinetic energy, equal to:

$$k = \frac{1}{2}\overline{u_i'u_i'}. \tag{2.34}$$

Although the eddy-viscosity hypothesis is not correct in detail, it is easy to implement and, with careful application, can provide reasonably good results for many flows. In the simplest description, turbulence can be characterized by two parameters: its kinetic energy, k, or a velocity, $q = \sqrt{2k}$, and a length scale, L, as for the mixing length model [35]. Dimensional analysis shows that:

$$\nu_T = C_\mu\rho q L, \tag{2.35}$$

where C_μ is a dimensionless constant. In the simplest practical models, k is determined from the mean velocity field using the approximation $q = L\partial u/\partial y$ and L is a prescribed function of the coordinates, easy to specify for simple flows but not for separated or highly three-dimensional flows. Mixing-length models can therefore be applied only to relatively simple flows; they are also known as zero equation models. Because a minimum description of turbulence requires at least a velocity scale and a length scale, a model which derives the needed quantities from two such equations is a logical choice. In almost all such models,

an equation for the turbulent kinetic energy, k, determines the velocity scale. The exact equation for this quantity is not difficult to derive:

$$
\begin{aligned}
\frac{\partial(\rho k)}{\partial t} + \frac{\partial\left(\rho \bar{u}_j k\right)}{\partial x_j} = & \frac{\partial}{\partial x_j}\left(\mu \frac{\partial k}{\partial x_j}\right) - \frac{\partial}{\partial x_j}\left(\frac{\rho}{2}\overline{u_j' u_i' u_i'} + \overline{p' u_j'}\right) - \\
& \rho \overline{u_i' u_j'} \frac{\partial \bar{u}_i}{\partial x_j} - \mu \overline{\frac{\partial u_i'}{\partial x_k} \frac{\partial u_i'}{\partial x_k}}
\end{aligned}
\tag{2.36}
$$

For details of the derivation of this equation see [34] or [45]. The terms on the left-hand side of this equation and the first term on the right-hand side need no modeling. The last term represents the product of the density ρ and the dissipation, ε, the rate at which turbulence energy is irreversibly converted into internal energy. The second term on the right-hand side represents turbulent diffusion of kinetic energy (which is actually transport of velocity fluctuations by the fluctuations themselves); it is almost always modeled by use of a gradient-diffusion assumption:

$$
-\left(\frac{\rho}{2}\overline{u_j' u_i' u_i'} + \overline{p' u_j'}\right) \approx \frac{\nu_\mathrm{T}}{\sigma_k}\frac{\partial k}{\partial x_j},
\tag{2.37}
$$

where σ_k is a turbulent Prandtl number whose value is approximately unity. The third term of the right-hand side represents the rate of production of turbulent kinetic energy by the mean flow, a transfer of kinetic energy from the mean flow to the turbulence. If we use the eddy-viscosity hypothesis, to estimate the Reynolds stress, it can be written:

$$
P_k = -\rho \overline{u_i' u_j'}\frac{\partial \bar{u}_i}{\partial x_j} \approx \nu_\mathrm{T}\left(\frac{\partial \bar{u}_i}{\partial x_j} + \frac{\partial \bar{u}_j}{\partial x_i}\right)\frac{\partial \bar{u}_i}{\partial x_j},
\tag{2.38}
$$

and, as the right hand-hand side of this equation can be calculated from quantities that will be computed, the development of the turbulent kinetic energy equation is complete. As mentioned above, another equation is required to determine the length scale of the turbulence. The choice is not obvious and a number of equations have been used for this purpose. The most popular one is based on the observations that the dissipation is needed in the energy equation and, in so-called equilibrium turbulent flows, i.e., ones in which the rates of production and destruction of turbulence are in near-balance, the dissipation ε, and k and L are related by:

$$
\varepsilon \approx \frac{k^{3/2}}{L}.
\tag{2.39}
$$

This idea is based on the fact, that at high Reynolds numbers, there is a cascade of energy from the largest scales to the smallest ones and that the energy transferred to the small
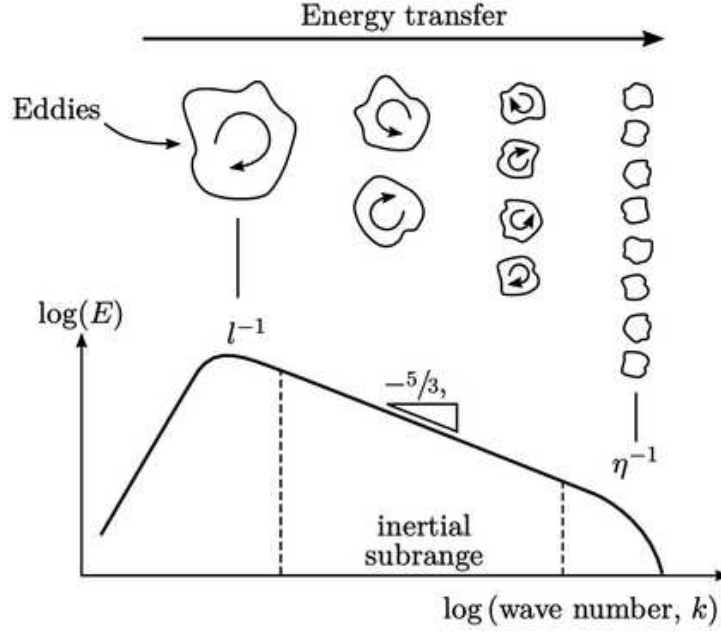
Figure 2.1.: Schematic illustration of production, energy cascade and dissipation in the energy spectrum of turbulence (picture taken from [18])

scales is dissipated, as shown in Fig. 2.1. It is also useful to introduce as a variable the specific rate of dissipation ω.

The SST k-ω turbulence model [26] is a two-equation eddy viscosity model which has become very popular. The shear stress transport (SST) formulation combines the best of two worlds. The use of a k-ω formulation in the inner parts of the boundary layer makes the model directly usable all the way down to the wall through the viscous sub-layer, hence the SST k-ω model can be used as a low-Re turbulence model without any extra damping functions. The SST formulation also switches to a k-ε behaviour in the free-stream and thereby avoids the common k-ω problem that the model is too sensitive to the inlet free-stream turbulence properties. For my study I will refer to the 2003 version of the model [25], the one implemented in the flow solver. The two equation model is given by the following:

$$
\begin{aligned}
\frac{D(\bar{\rho}k)}{Dt} &= \bar{\rho}P_k - \beta^*\bar{\rho}\omega k + \frac{\partial}{\partial x_i}\left[(\mu + \sigma_k \nu_T)\frac{\partial k}{\partial x_i}\right] \\
\frac{D(\bar{\rho}\omega)}{Dt} &= \gamma\frac{\bar{\rho}^2}{\nu_T}P_k - \beta\bar{\rho}\omega^2 + \frac{\partial}{\partial x_i}\left[(\mu + \sigma_\omega \nu_T)\frac{\partial \omega}{\partial x_i}\right] + 2\left(1 - F_1\right)\frac{\sigma_{\omega 2}\bar{\rho}}{\omega}\frac{\partial k}{\partial x_i}\frac{\partial \omega}{\partial x_i}
\end{aligned}
\tag{2.40}
$$

and the turbulent production $\bar{\rho}P_k = 1/2\bar{\rho}P_{ii}$ is obtained by substituting the Boussinesq assumption into the production term of Reynolds stresses and taking the trace. It is limited to values smaller than 10 times the destruction of turbulent kinetic energy. Menter's rationale was to produce an ω-equation, which he called BSL-ω , that behaves like an ω-equation close to solid walls and like an ε-equation in free shear flows. For this reason,

Table 2.1.: SST k-ω model equations coefficients

Constant	β	σ_k	σ_ω	γ
Inner layer (1)	0.075	0.85	0.5	0.556
Outer layer (2)	0.0828	1.0	0.856	0.44

all constants ϕ in the equations are blended by his F_1 function via:

$$\phi = F_1 \phi_1 + (1 - F_1)\,\phi_2. \tag{2.41}$$

All the constants are given in Tab. 2.1, distinguishing values according to the region they refer to:

The remaining coefficient is $\beta^* = 0.09$. The turbulent eddy viscosity is computed from:

$$\nu_T = \frac{\rho a_1 k}{\max\left(a_1 \omega,\, S F_2\right)} \tag{2.42}$$

with $a_1 = 0.31$ and the strain norm $S = \sqrt{S_{ij} S_{ij}}$, that is the reason behind the model being addressed as shear stress transport (SST). It is based on the Bradshaw assumption that the shear stress is proportional to the turbulent kinetic energy in equilibrium boundary layers [5].

The blending functions F_1 and F_2 are rather complex functions of turbulence quantities, viscosity and distance to the wall. They are given by:

$$F_1 = \tanh\left(\mathrm{arg}_1^4\right)$$
$$\mathrm{arg}_1 = \min\left[\max\left(\frac{\sqrt{k}}{\beta^* \omega d},\, \frac{500\mu}{\bar{\rho} d^2 \omega}\right),\, \frac{4\bar{\rho}\sigma_{\omega 2} k}{CD_{k\omega} d^2}\right] \tag{2.43}$$
$$CD_{k\omega} = \max\left(\frac{2\bar{\rho}\sigma_{\omega 2}}{\omega}\frac{\partial k}{\partial x_i}\frac{\partial \omega}{\partial x_i},\, 10^{-10}\right)$$

and:

$$F_2 = \tanh\left(\mathrm{arg}_2^2\right)$$
$$\mathrm{arg}_2 = \max\left(\frac{2\sqrt{k}}{\beta^* \omega d},\, \frac{500\mu}{\bar{\rho} d^2 \omega}\right) \tag{2.44}$$

The flow solver allows the user to adopt a wide range of modifications to the model, which for time and space reasons are not going to be discussed here, but if interested in the matter, it is possible to find additional information in the flow solver user guide [36].

2.2.2. RSMs and SSG/LRR-ω Model

Eddy-viscosity based models like the k-ε and the k-ω models have significant shortcomings in complex, real-life turbulent flows. For instance, in flows with streamline curvature, flow separation, flows with zones of re-circulating flow or flows influenced by mean rotational effects, the performance of these models is unsatisfactory. Such one- and two-equation based closures cannot account for the return to isotropy of turbulence, observed in decaying turbulent flows. Eddy-viscosity based models cannot replicate the behaviour of turbulent flows in the Rapid Distortion limit, where the turbulent flow essentially behaves as an elastic medium (instead of viscous).

The most complete classical turbulence models nowadays are Reynolds stress equation model (RSM), also referred to as second moment closures. In these models, the eddy-viscosity hypothesis is avoided and the individual components of the Reynolds stress tensor are directly computed. These models use the exact Reynolds stress transport equation for their formulation. They account for the directional effects of the Reynolds stresses and the complex interactions in turbulent flows. Reynolds stress models offer significantly better accuracy than eddy-viscosity based turbulence models, while still remaining computationally cheaper than DNS and LES. The Reynolds stress model involves calculation of the individual Reynolds stresses, $\rho \overline{u'_i u'_j}$, using differential transport equations. The individual Reynolds stresses are then used to obtain closure of the Reynolds-averaged momentum equation. The exact transport equations for the transport of the Reynolds stresses can be written as follows:

$$\frac{\partial}{\partial t}\left(\rho \overline{u'_i u'_j}\right) + C_{ij} = D_{T,ij} + D_{L,ij} + P_{ij} + \phi_{ij} - \varepsilon_{ij} + F_{ij}, \qquad (2.45)$$

where C_{ij} is the convection term, $D_{T,ij}$ equals the turbulent diffusion, $D_{L,ij}$ stands for the molecular diffusion, P_{ij} is the term for stress production, ϕ_{ij} is for the pressure strain, ε_{ij} stands for the dissipation and F_{ij} is the production by system rotation. Between these terms C_{ij}, $D_{L,ij}$, P_{ij}, and F_{ij} do not require modelling. However, $D_{T,ij}$, ϕ_{ij}, and ε_{ij} have to be modelled for closing the equations. The fidelity of the Reynolds stress model depends on the accuracy of the models for the turbulent transport, the pressure-strain correlation and the dissipation terms. Additional information on the above-mentioned terms can be found in [41] and [9].

Now, strictly regarding the SSG/LRR-ω a slightly different formulation of the Reynolds stress transport equation is going to be used:

$$\frac{\partial \left(\bar{\rho} \widetilde{R}_{ij} \right)}{\partial t} + \frac{\partial}{\partial x_i} \left(\bar{\rho} \widetilde{R}_{ij} \widetilde{u}_i \right) = \bar{\rho} P_{ij} + \bar{\rho} \Pi_{ij} - \bar{\rho} \varepsilon_{ij} + \bar{\rho} D_{ij}, \tag{2.46}$$

where $\bar{\rho} \widetilde{R}_{ij}$ are the Cartesian components of the Reynolds stress tensor. The Cartesian components of the production term are given by:

$$\bar{\rho} P_{ij} = -\bar{\rho} \widetilde{R}_{ik} \frac{\partial \widetilde{u}_j}{\partial x_k} - \bar{\rho} \widetilde{R}_{jk} \frac{\partial \widetilde{u}_i}{\partial x_k}, \tag{2.47}$$

and, as said before they, they do not need modeling since all quantities are provided by the system of equations to be solved. The Cartesian components of the pressure-strain correlation are formally modeled according to Speziale, Sarkar and Gatski (SSG) [15] as:

$$\bar{\rho} \Pi_{ij} = - \left(C_1 \bar{\rho} \varepsilon + \frac{1}{2} C_1^* \bar{\rho} P_{ii} \right) \widetilde{b}_{ij} + C_2 \bar{\rho} \varepsilon \left(\widetilde{b}_{ik} \widetilde{b}_{kj} - \frac{1}{3} \widetilde{b}_{kl} \widetilde{b}_{kl} \delta_{ij} \right) + \left(C_3 - C_3^* \sqrt{\widetilde{b}_{kl} \widetilde{b}_{kl}} \right) \bar{\rho} \widetilde{k} \widetilde{S}_{ij}^*$$
$$+ C_4 \bar{\rho} \widetilde{k} \left(\widetilde{b}_{ik} \widetilde{S}_{jk} + \widetilde{b}_{jk} \widetilde{S}_{ik} - \frac{2}{3} \widetilde{b}_{kl} \widetilde{S}_{kl} \delta_{ij} \right) + C_5 \bar{\rho} \widetilde{k} \left(\widetilde{b}_{ik} \widetilde{\Omega}_{jk} + \widetilde{b}_{jk} \widetilde{\Omega}_{ik} \right), \tag{2.48}$$

where $\widetilde{k} = \widetilde{R}_{ii}/2$ is the specific kinetic turbulence energy and

$$\widetilde{b}_{ij} = \frac{\widetilde{R}_{ij}}{2\widetilde{k}} - \frac{1}{3} \delta_{ij}, \tag{2.49}$$

represents the Cartesian components of the anisotropy tensor. Furthermore there are:

$$\widetilde{S}_{ij} = \frac{1}{2} \left(\frac{\partial \widetilde{u}_i}{\partial x_j} + \frac{\partial \widetilde{u}_j}{\partial x_i} \right),$$
$$\widetilde{S}_{ij}^* = \widetilde{S}_{ij} - \frac{1}{3} \widetilde{S}_{ii} \delta_{ij}, \tag{2.50}$$
$$\widetilde{\Omega}_{ij} = \frac{1}{2} \left(\frac{\partial \widetilde{u}_i}{\partial x_j} - \frac{\partial \widetilde{u}_j}{\partial x_i} \right),$$

denoting the Cartesian components of the simple strain rate tensor, the traceless strain rate tensor and the rotation tensor, respectively. The C_i and C_i^* are model dependent coefficients. Dissipation is modeled as an isotropic tensor with Cartesian components:

$$\bar{\rho} \varepsilon_{ij} = \frac{2}{3} \bar{\rho} \varepsilon, \tag{2.51}$$

where the isotropic dissipation rate ε is provided indirectly by a transport equation for the specific dissipation rate ω given further below. Two different models are available representing non-convective fluxes, simple gradient diffusion:

$$\bar{\rho}D_{ij} = \frac{\partial}{\partial x_i}\left[\left(\bar{\mu} + \frac{D^{(SD)}}{C_\mu}\frac{\bar{\rho}\widetilde{k}^2}{\varepsilon}\right)\frac{\partial \widetilde{R}_{ij}}{\partial x_i}\right], \tag{2.52}$$

or generalized gradient diffusion:

$$\bar{\rho}D_{ij} = \frac{\partial}{\partial x_i}\left[\left(\bar{\mu}\delta_{ij} + D^{(GD)}\frac{\bar{\rho}\widetilde{k}\widetilde{R}_{kl}}{\varepsilon}\right)\frac{\partial \widetilde{R}_{ij}}{\partial x_i}\right], \tag{2.53}$$

where $\bar{\mu}$ is the mean dynamic fluid viscosity and $D^{(SD)}$ and $D^{(GD)}$ represent respective model coefficients. Finally, Menter's baseline equation, in a slightly different formulation from the one previously given:

$$\frac{\partial(\bar{\rho}\omega)}{\partial t} + \frac{\partial}{\partial x_i}\left(\bar{\rho}\omega\widetilde{U}_k\right) = \gamma\frac{\omega}{\widetilde{k}}\frac{\bar{\rho}P_{kk}}{2} - \beta\bar{\rho}\omega^2 + \frac{\partial}{\partial x_i}\left[\left(\bar{\mu} + \sigma_\omega\frac{\bar{\rho}\widetilde{k}}{\omega}\right)\frac{\partial\omega}{\partial x_i}\right] + \sigma_k\frac{\bar{\rho}}{\omega}\max\left(\frac{\partial\widetilde{k}}{\partial x_i}\frac{\partial\omega}{\partial x_i}, 0\right), \tag{2.54}$$

is employed for providing the isotropic dissipation rate $\varepsilon = C_\mu\widetilde{k}\omega$ where $C_\mu = 0.09$. As with the SST model, the coefficients $\phi = \gamma, \beta, \sigma_\omega, \sigma_k$ are blended according to:

$$\phi = F_1\phi_1 + (1 - F_1)\phi_2, \tag{2.55}$$

between the bounding values associated with the ω-equation by Wilcox near walls ($F_1 = 1$) and the standard ε-equation at the boundary layer edge ($F_1 = 0$), where the blending function is given by:

$$F_1 = \tanh\left(\zeta^4\right), \tag{2.56}$$

with the argument:

$$\zeta = \min\left[\max\left(\frac{\sqrt{\widetilde{k}}}{C_\mu\omega d}, \frac{500\bar{\mu}}{\bar{\rho}\omega d^2}\right), \frac{4\sigma_{\omega 2}\bar{\rho}\widetilde{k}}{\sigma_{k2}\frac{\bar{\rho}}{\omega}\max\left(\frac{\partial\widetilde{k}}{\partial x_i}\frac{\partial\omega}{\partial x_i}, 0\right)d^2}\right], \tag{2.57}$$

based on the wall-distance d. The corresponding values of the coefficients are given in Tab. 2.2.

Table 2.2.: Menter's BSL equation coefficients for SSG/LRR-ω

	β	σ_k	σ_ω	γ
Inner layer (1)	0.075	0	0.5	0.556
Outer layer (2)	0.0828	1.712	0.856	0.44

The fundamental idea of the SSG/LRR-ω model is to combine the ε-based SSG model for the pressure strain correlation with the simpler model by Launder, Reece and Rodi (LRR) near walls in the ω-based formulation of Wilcox (see [20]). Since the LRR-model can be written as a subset of the above SSG-model, the same blending of the Reynolds stress model coefficients $C_i, C_i^*, D^{(SD)}$ and $D^{(GD)}$ can be applied as to the coefficients of the ω-equation. Thus, all coefficients change consistently from LRR $+ \omega$ near walls to SSG $+ \varepsilon$ at the boundary layer edge. The corresponding bounding values are given in Tab. 2.3. Note that the value of the coefficient $c_2^{(LRR)}$ as well as the generalized diffusion coefficient $D^{(GD)}$ have been re-calibrated for better agreement with the log-law velocity profile in a zero pressure gradient boundary layer.

Table 2.3.: Bounding values of the SSG/LRR-ω model term coefficients $\left(c_2^{(LRR)} = 0.52 \right)$

	C_1	C_1^*	C_2	C_3	C_3^*	C_4	C_5	$D^{(SD)}$	$D^{(GD)}$
SSG	3.4	1.8	4.2	0.8	1.3	1.25	0.4	$\frac{2}{3}$0.22	0.22
LRR	3.6	0	0	0.8	0	$\frac{18c_2^{(LRR)}+12}{11}$	$\frac{-14c_2^{(LRR)}+20}{11}$	$0.5C_\mu$	$0.75C_\mu$

In the end for a wide range of separated flows the SSG/LRR-ω model yields similar results as the Spalart-Allmaras or the SST models. Advantages have been observed with respect to the prediction of the shock position and the length of separation bubbles. However, the reverse flow speed inside the bubble seems to be generally underestimated. Furthermore, effects of streamline curvature and secondary flow are predicted reasonably well by the SSG/LRR-ω model. Capturing these effects requires curvature corrections or nonlinear extensions in standard eddy-viscosity models. Thus, the SSG/LRR-ω model appears to have a wider range of applicability than eddy-viscosity models without special modifications [10].

2.3. Overview of Large-Eddy Simulation

Turbulent flows contain a wide range of length and time scales; the range of eddy sizes that might be found in a flow is shown schematically on the left-hand side of Fig. 2.2. The right-hand side of this figure shows the time history of a typical velocity component at a point in the flow; the range of scales on which fluctuations occur is obvious. The large scale motions are generally much more energetic than the small scale ones and are directly affected by the boundary conditions; their size and strength make them by far the most effective transporters of the conserved properties and so they are usually computed.
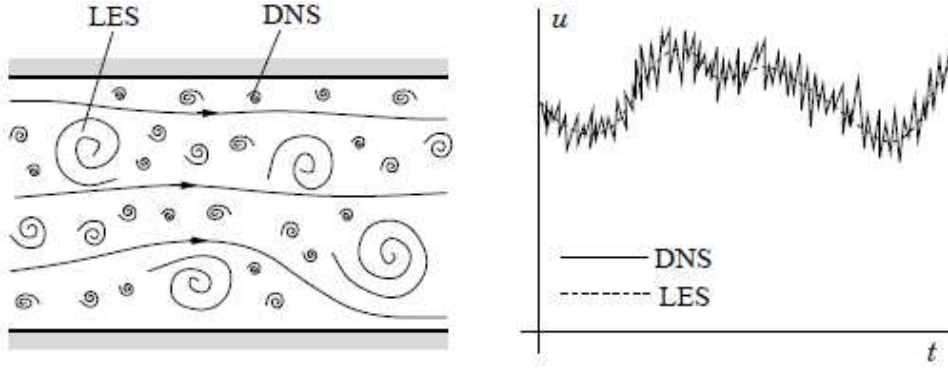
Figure 2.2.: Schematic representation of turbulent motion (left) and the time-dependence of a velocity component at a point (right) (picture taken from [13])

The small scales are usually much weaker and provide little transport of these properties. Also, they are roughly isotropic and have nearly universal characteristics; it is thus more amenable to modeling. Thus, a method which resolves the large energy containing motions and models the small ones, may make sense.

Large-eddy simulation (LES) is just such an approach, as they are a method in which the large eddies are computed and the smallest, subgrid-scale (SGS), eddies are modeled. It is essential to define the quantities to be computed precisely. Field variables that contains only the large scale components of the total field are needed. This is best produced by filtering the various quantities; in this approach, the large or resolved scale field, the one to be simulated, is essentially a local average of the complete field. Any filtered variable can be defined by:

$$\bar{A}(\boldsymbol{x},t) = \int_{R^3} G_\Delta(\boldsymbol{r}) A(\boldsymbol{x} - \boldsymbol{r},t) \mathrm{d}r^3, \tag{2.58}$$

where $G_\Delta(\boldsymbol{r})$, the filter kernel, is a localized function and satisfies the following property:

$$\int_{R^3} G_\Delta(r) \mathrm{d}r^3 = 1 \tag{2.59}$$

Filter kernels which have been applied in LES include a Gaussian, a box filter (a simple local average) and a cutoff (a filter which eliminates all Fourier coefficients belonging to wavenumbers above a cutoff). Every filter has a length scale associated with it, Δ. Roughly, eddies larger than Δ are are resolved while structures smaller than Δ need to be modeled. Any flow variable can be decomposed into a filtered (large-scale, resolved) part $\bar{A}$ and into a sub-filter (unresolved) part A' as:

$$A = \bar{A} + A'. \tag{2.60}$$

As done for RANS, the spatial filtering has to be applied to the Navier-Stokes equations

in order to remove the small turbulent scales. The filter width Δ, as well as the filter function are considered as free parameters. In fact, the governing equations are usually not explicitly filtered. Instead, the grid as well as the discretization errors are assumed to define the filter G. For compressible flows the spatial filtering has to be applied together with the Favre averaging, otherwise the filtered Navier-Stokes equations would contain products between density and other variables like velocity or temperature. Thus, velocity components, energy and temperature are decomposed as:

$$A = \widetilde{A} + A''. \tag{2.61}$$

It is important to notice that unlike for RANS:

$$\widetilde{\widetilde{A}} \neq \widetilde{A} \tag{2.62}$$

Applying the filtering operations on the dimensionless conservation laws, (for further details see [16]) the filtered Navier-Stokes equations can be obtained:

$$\frac{\partial \bar{\rho}}{\partial t} = -\frac{\partial}{\partial x_j} \left(\bar{\rho} \widetilde{u}_j \right), \tag{2.63}$$

$$\frac{\partial \bar{\rho} \widetilde{u}_i}{\partial t} = -\frac{\partial}{\partial x_j} \left(\bar{\rho} \widetilde{u}_i \widetilde{u}_j \right) - \frac{\partial}{\partial x_i} \bar{p} + \left[\frac{\partial}{\partial x_j} \hat{\tau}_{ij} - \frac{\partial}{\partial x_j} \bar{\rho} a_{ij} \right] + \left[\frac{\partial}{\partial x_j} (\widetilde{\tau}_{ij} - \hat{\tau}_{ij}) \right], \tag{2.64}$$

where $\hat{\tau}_{ij}$ is the stress tensor based on $\widetilde{T}$ and $\widetilde{\boldsymbol{u}}$ and the quantity a_{ij} is here used to define the Reynolds stress tensor:

$$a_{ij} = \widetilde{u_i u_j} - \widetilde{u}_i \widetilde{u}_j. \tag{2.65}$$

In the filtered energy equation a modified total energy $\hat{e}$ is introduced, which is the total energy based on the filtered variables:

$$\hat{e} = \frac{\bar{p}}{\gamma - 1} + \frac{1}{2} \bar{\rho} \widetilde{u}_i \widetilde{u}_i = \bar{e} + \frac{1}{2} \bar{\rho} a_{ii}. \tag{2.66}$$

The $\hat{e}$-equation is obtained when the bar-filter is applied to the energy equation and the transport equation for the turbulent kinetic energy ($\bar{\rho} a_{kk}/2$) is subtracted. After a lengthy calculation one obtains:

$$\frac{\partial \hat{e}}{\partial t} = - \left(\frac{\partial \left((\hat{e} + \bar{p}) \widetilde{u}_j \right)}{\partial x_j} \right)$$
$$+ \left[\frac{\partial \left(\hat{\tau}_{ij} \widetilde{u}_i \right)}{\partial x_j} - \frac{\partial \hat{q}_j}{\partial x_j} - \frac{1}{\gamma - 1} \frac{\partial \left(\overline{p u_j} - \bar{p} \widetilde{u}_j \right)}{\partial x_j} - \left(\overline{p \frac{\partial u_k}{\partial x_k}} - \bar{p} \frac{\partial \widetilde{u}_k}{\partial x_k} \right) - \frac{\partial \left(\bar{\rho} a_{kj} \widetilde{u}_k \right)}{\partial x_j} \right] \quad (2.67)$$
$$+ \left[\bar{\rho} a_{kj} \frac{\partial \widetilde{u}_k}{\partial x_j} + \overline{\tau_{kj} \frac{\partial u_k}{\partial x_j}} - \bar{\tau}_{kj} \frac{\partial \widetilde{u}_k}{\partial x_j} + \frac{\partial \left(\bar{\tau}_{ij} \widetilde{u}_i - \hat{\tau}_{ij} \widetilde{u}_i \right)}{\partial x_j} - \frac{\partial \left(\bar{q}_j - \hat{q}_j \right)}{\partial x_j} \right]$$

in which even the heat flux $\hat{q}$ is based on the variable $\widetilde{T}$. The derived system of equations contains terms which can directly be identified with the unfiltered Navier-Stokes equations but also several additional nonlinear contributions (subgrid-terms) appear as well which cannot be directly related to the filtered flow quantities. If these equations are used as the basis for LES, usually only the quantities a_{ij} and $\partial \left(\overline{p u_j} - \bar{p} \widetilde{u}_j \right) / \partial x_j$ are replaced by a model representation whereas the other nonlinear subgrid terms are simply disregarded.

The modeling of the subgrid scale tensor $\bar{\tau}_{ij} = \bar{u}_i \bar{u}_j - \overline{u_i u_j}$ is usually based on an eddy-viscosity assumption as:

$$\bar{\tau}_{ij} - \frac{1}{3} \bar{\tau}_{kk} \delta_{ij} = 2 \nu_T \bar{S}_{ij}, \quad (2.68)$$

where:

$$\bar{S}_{ij} = \frac{1}{2} \left(\frac{\partial \bar{u}_i}{\partial x_j} + \frac{\partial \bar{u}_j}{\partial x_i} \right), \quad (2.69)$$

is the deformation tensor of the resolved field. Different models for the subgrid stresses are available. Due to the spatial filtering, the models below all use the cell size $\Delta = V^{\frac{1}{3}}$ where V is the cell volume.
One of the earliest formulated model is the Smagorinsky one [40], in which the eddy-viscosity is assumed to be proportional to the subgrid length scale Δ and to the norm of the strain tensor via:

$$\nu_T = \bar{\rho} \left(C_s \Delta \right)^2 \sqrt{2 \bar{S}_{ij} \bar{S}_{ij}}, \quad (2.70)$$

with the constant $C_S = 0.17$.

The model adopted in the current study is the wall adaptive local eddy viscosity or WALE model, implemented according to [31]. Like the Smagorinsky model it determines an eddy viscosity locally from resolved quantities. It is now useful to define the following quantities:

$$\bar{\Omega}_{ij} = \frac{1}{2}\left(\frac{\partial \bar{u}_i}{\partial x_j} - \frac{\partial \bar{u}_j}{\partial x_i}\right), \tag{2.71}$$

and:

$$S_{ij}^d = \bar{S}_{ik}\bar{S}_{kj} + \bar{\Omega}_{ik}\bar{\Omega}_{kj} - \frac{1}{3}\delta_{ij}\left[\bar{S}_{mn}\bar{S}_{mn} - \bar{\Omega}_{mn}\bar{\Omega}_{mn}\right]. \tag{2.72}$$

This way we can obtain the eddy-viscosity formulation according to the WALE model, which is:

$$\nu_T = (C_w \Delta)^2 \frac{\left(f_{ij}^d f_{ij}^d\right)^{3/2}}{\left(\bar{S}_{ij}\bar{S}_{ij}\right)^{5/2} + \left(S_{ij}^d S_{ij}^d\right)^{5/4}}, \tag{2.73}$$

where the constant $C_w = 0.5587$ is computed from the relation:

$$C_w^2 = \alpha C_s^2, \tag{2.74}$$

and C_s has the same value as for Smagorinsky model while the factor α is found through averaging several values related to different turbulent fields (see [31]). The resulting formulation ensures some advantages compared to the classical Smagorinsky formulation, for example, all the turbulence structures relevant for the kinetic energy dissipation are detected. Moreover, the eddy-viscosity tends to go naturally to zero in the vicinity of a wall, removing the need for any dynamic constant adjustment or damping functions in the computation of wall-bounded flows. As the model produces zero eddy viscosity in case of a pure shear, it is able to reproduce the laminar to turbulent transition process through the growth of linear unstable modes. Finally, the model is invariant to any coordinate translation or rotation, meaning that it can be used for complex geometries.

2.4. Turbulent Wake Flows

In these paragraph, the formation and description of turbulent wake flows is going to be discussed. The wake is the region of disturbed flow, downstream of a body caused by the flowing of a fluid around it. This phenomenon is originated when the development of the boundary layer over the surface of a body leads, under certain conditions, to its separation.
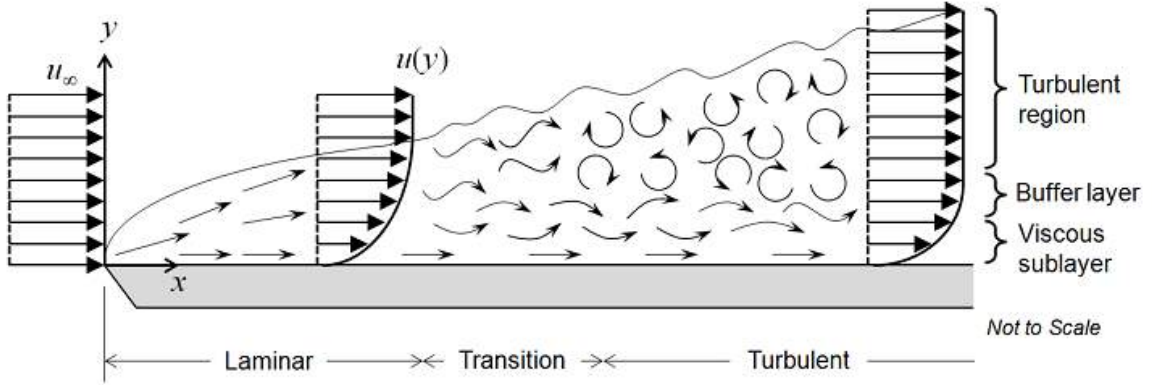

Figure 2.3.: Boundary layer development for a flow over a flat plate (picture taken from [32])

To better understand this mechanism, the simplest case of a boundary layer formation on a flat plate is going to be initially examined. Consider a uniform-velocity, non-turbulent stream flow over a smooth, semi-infinite, flat plate (i.e the wall) laying on the $x - z$ plane; the mean flow is predominantly in the x direction and the free-stream velocity (outside the boundary layer) can be denoted by $u_\infty(x)$. Statistics vary primarily in the y direction, that is the distance from the wall, and are independent of z but as the boundary layer continually develops, they depend both upon x and upon y. The velocity components are u, v, and w. The free-stream pressure $p_\infty(x)$ is linked to the velocity $u_\infty(x)$ by Bernoulli's equation $-p_\infty(x) + \frac{1}{2}\rho u_\infty^2(x) = constant$, so that the pressure gradient is:

$$-\frac{\mathrm{d}p_\infty}{\mathrm{d}x} = \rho u_\infty \frac{\mathrm{d}u_\infty}{\mathrm{d}x}. \tag{2.75}$$

Accelerating flows are defined according to:

$$\frac{\mathrm{d}u_\infty}{\mathrm{d}x} > 0, \tag{2.76}$$

and corresponds to a negative (favorable) pressure gradient. Conversely, decelerating flows yields a positive (adverse) pressure gradient, so called because it can lead to separation of the boundary layer from the surface and they are, conversely, determined by:

$$\frac{\mathrm{d}u_\infty}{\mathrm{d}x} < 0. \tag{2.77}$$

It is useful to specify another variable, namely the local Reynolds number, which is strictly related to the state regime of the flow over the plate:

$$\mathrm{Re}_x \equiv \frac{u_\infty x}{\nu}. \tag{2.78}$$

In a zero-pressure-gradient boundary layer, there is laminar flow from the leading edge ($x = 0$) until the location at which Re_x reaches a critical value $\mathrm{Re}_{\mathrm{crit}} \approx 10^6$ marking the start of transition. The value of $\mathrm{Re}_{\mathrm{crit}}$ varies considerably, depending on the nature and level of the disturbances in the free stream, see, e.g., [38]. Transition occurs over some distance, after which the boundary layer is fully turbulent as shown in Fig. 2.3. The boundary layer thickness, δ, can be defined as the height above the surface where the flow velocity on the boundary layer approaches the external flow velocity $u_\infty(x)$; δ grows progressively and asymptotically, meaning that its growth rate is initially significant, and then the growth rate slows down as the boundary layer develops further downstream.
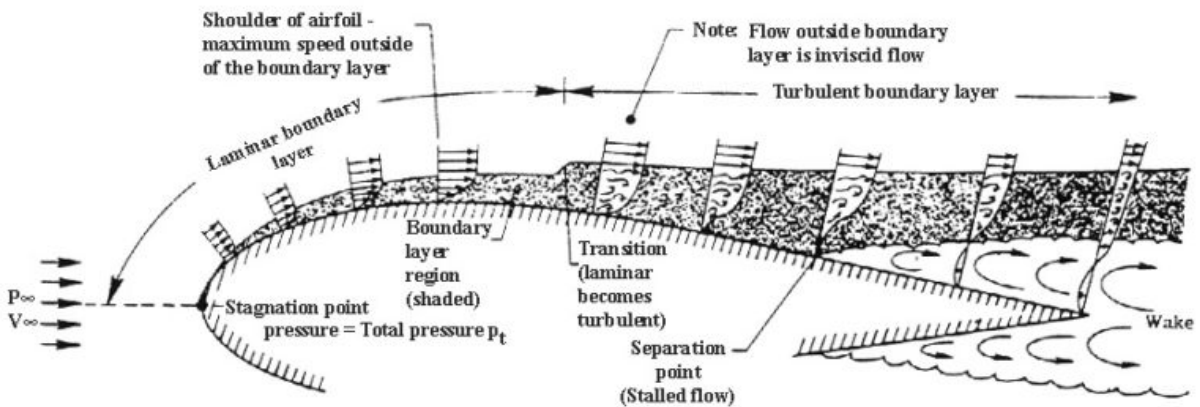

Figure 2.4.: Boundary layer separation over the suction surface of an airfoil (picture taken from [3])

In the previous part the considered body was an ideal plate but for the purpose of the research a LPT blade was studied, so a body which in addition to the plate characteristics possess a curvature, along the dominant flow direction. On the upper (suction) surface of an airfoil the curvature is convex; whereas there is concave curvature over part of the lower (pressure) surface of a cambered airfoil. In the flow over airfoils, the boundary layer is simultaneously subjected to the effects of curvature and a mean pressure gradient. Focusing on the suction side, as the velocity decreases, the adverse pressure gradient over the back half slows down the boundary layer flow, especially near the surface, and causes it to separate. This happens at a position where the boundary layer profile develops a point of inflection, so the corresponding wall shear stress becomes:

$$\tau_w = \mu \left(\frac{\mathrm{d}u}{\mathrm{d}y} \right)_{wall} = 0. \tag{2.79}$$

The flow reverses, a region of recirculating flow develops and the thickness of the boundary layer abruptly increases and the layer is forced off the surface, see Fig. 2.4. This, in the end, causes the formation of a turbulent wake with the presence of vortical structures that finally leads to aerodynamics problems and energy losses.

2.5. Entropy Loss Generation for RANS and LES

The purpose of this section is to give an outline on the main method that is used in the analysis of loss generation for the studied case. An efficient use of energy is one of the most important goals in modern turbomachinery design. Based on the second law of thermodynamics, entropy generation is being widely used to represent loss of efficiency. Generally, viscous effects and irreversible heat flux are taken as major sources for entropy generation in turbomachinery, and various empirical relations have been derived to estimate the entropy generated from different origins such as the viscous effects in the boundary layer, viscous effects in wake mixing, and heat transfer across temperature differences. In the past years, several studies have been carried out to quantify entropy generation through CFD calculations, as for example the one by Moore and Moore [27] or more recently the paper from Lengani et al.[21]. For our case study we will focus on the paper by Zhao et al. [46] as the performed procedure is based on the same approach.

From the second law of thermodynamics, the total entropy S follows:

$$\dot{S} + I_S = \int_V G_s dV \geq 0, \tag{2.80}$$

with $\dot{S}$ the time rate of change of the system entropy, I_S is the entropy current with external environment, and the right-hand side term represents the entropy generation rate G_s integrated over the volume V. For most thermodynamic processes the generation of total entropy is greater than zero, while the equivalent holds only when the process is reversible. For single phase fluid flows, it can be written:

$$\frac{\partial(\rho s)}{\partial t} + \frac{\partial F_i}{\partial x_i} \equiv G_s \geq 0, \tag{2.81}$$

where s is the specific entropy and F_i is the entropy flux caused by mass flux and heat transfer.

Starting from RANS equations, after some calculations it is possible to derive the entropy balance equation for the mean flow:

$$\frac{\partial \left(\bar{\rho}\tilde{u}_i\tilde{s}\right)}{\partial x_i} + \frac{\partial}{\partial x_i}\left(\frac{\tilde{q}_i}{\tilde{T}}\right) = \frac{1}{\tilde{T}}\tau_{ij}(\tilde{u})\frac{\partial \tilde{u}_j}{\partial x_i} + \frac{c_p\mu}{\mathrm{Pr}}\frac{1}{\tilde{T}^2}\left(\frac{\partial \tilde{T}}{\partial x_i}\right)^2$$
$$+ \frac{1}{\tilde{T}}\tau_{ij}^R\frac{\partial \tilde{u}_j}{\partial x_i} - \frac{1}{\tilde{T}}\frac{\partial}{\partial x_i}\left(q_i^R\right) - \frac{1}{\tilde{T}}\frac{\partial \left(\bar{\rho}\tilde{u}_i k\right)}{\partial x_i} \qquad (2.82)$$

where the turbulent heat flux is here defined as:

$$q_j^R = \bar{\rho}c_p\left(\widetilde{Tu_j} - \tilde{T}\tilde{u}_j\right). \qquad (2.83)$$

The left hand side of entropy balance equation represents entropy variations caused by mass and heat fluxes with external environments. On the right-hand side, the entropy generation mechanisms for RANS flow fields can be written as:

$$\tilde{G}_s^{RANS} = \underbrace{\frac{1}{\tilde{T}}\tau_{ij}(\tilde{u})\frac{\partial \tilde{u}_j}{\partial x_i}}_{V_M} + \underbrace{\frac{c_p\mu}{\mathrm{Pr}}\frac{1}{\tilde{T}^2}\left(\frac{\partial \tilde{T}}{\partial x_i}\right)^2}_{H_M}$$
$$+ \underbrace{\frac{1}{\tilde{T}}\tau_{ij}^R\frac{\partial \tilde{u}_j}{\partial x_i}}_{P_R} - \underbrace{\frac{1}{\tilde{T}}\frac{\partial}{\partial x_i}\left(q_i^R\right)}_{H_R} - \underbrace{\frac{1}{\tilde{T}}\frac{\partial \left(\bar{\rho}\tilde{u}_i k\right)}{\partial x_i}}_{A_k}, \qquad (2.84)$$

which include entropy generation caused by the mean viscous dissipation V_M, mean flow irreversible heat flux H_M, the turbulence production related to the Reynolds stress P_R, turbulent heat flux H_R, and advection of turbulent kinetic energy (TKE) A_k. We remark that the terms P_R, H_R, and A_k stand for the contribution of turbulence fluctuations to the irreversible process of entropy generation.

In a similar way the same procedure can be applied to LES equations obtaining a comparable equation for the entropy generation with the only difference being in two additional SGS terms:

$$\tilde{G}_s^{LES} = \underbrace{\frac{1}{\tilde{T}}\tau_{ij}(\tilde{u})\frac{\partial \tilde{u}_j}{\partial x_i}}_{V_M} + \underbrace{\frac{c_p\mu}{\mathrm{Pr}}\frac{1}{\tilde{T}^2}\left(\frac{\partial \tilde{T}}{\partial x_i}\right)^2}_{H_M}$$
$$+ \underbrace{\frac{1}{\tilde{T}}\tau_{ij}^R\frac{\partial \tilde{u}_j}{\partial x_i}}_{P_R} - \underbrace{\frac{1}{\tilde{T}}\frac{\partial}{\partial x_i}\left(q_i^R\right)}_{H_R} - \underbrace{\frac{1}{\tilde{T}}\frac{\partial \left(\bar{\rho}\tilde{u}_i k\right)}{\partial x_i}}_{A_k} \qquad (2.85)$$
$$+ \underbrace{\frac{1}{\tilde{T}}\tau_{ij}^{\mathrm{SGS}}\frac{\partial \tilde{u}_j}{\partial x_i}}_{V_S} - \underbrace{\frac{1}{\tilde{T}}\frac{\partial}{\partial x_i}\left(q_i^{\mathrm{SGS}}\right)}_{H_S},$$

where V_S and H_S represent the entropy generation related to the viscous dissipation caused by SGS stress and the SGS heat flux. These two last mentioned variables are defined as:

$$
\begin{aligned}
\tau_{ij}^{\text{SGS}} &= -\bar{\rho}\left(\overline{u_i u_j} - \bar{u}_i \bar{u}_j\right) \\
q_j^{\text{SGS}} &= \bar{\rho} c_p \left(\overline{T u_j} - \bar{T}\bar{u}_j\right).
\end{aligned}
\tag{2.86}
$$

3. Test Case Configuration and Simulations Setup

In this chapter, an overview of the MTU-T161 LPT cascade characteristics is given. Afterwards, the numerical setup of the simulation is described for both RANS and LES simulations. For the former, the description is split between the full blade setup and the wake setup, while for the latter only the entire setup is considered. Moreover, for the RANS wake setup simulations, the procedure to extract suitable boundary conditions is reported. Finally, in the last part of the chapter, the softwares used throughout the research are briefly discussed.

3.1. MTU-T161 LPT Cascade

The subject of all the researches and simulations carried out in the context of this work is the MTU-T161 test case; the three-dimensional turbine passage is illustrated in Fig. 3.1.

The salient characteristic of the MTU-T161 is the presence of diverging conical end-walls, designed to promote three-dimensionality in the flow and induce realistic conditions, relevant to rotating machines. The case also features a revised high-lift profile with improved blade-loading representative of modern turbine designs. The flow around a linear turbine cascade with sidewalls needs to be simulated. The corresponding experimental setup consist of a cascade with seven linear blades. The numerical simulation is concerned with describing the flow around the mid turbine blade. Hence, it is sufficient to setup the simulation as a one blade setup and apply periodic boundary conditions in the pitch wise direction to mimic the interaction of the flow with the neighboring blades. For what concerns the spanwise direction, to account for the diverging sidewalls of the cascade, even the computational domain possesses inclined external walls with respect to the flow direction. At Re=90 000 both LES and experimental data are available, while at Re=200 000 only experimental data are taken into account, since LES does not match them. For the higher Reynolds number case, only the RANS simulations of the full blade setup are performed.
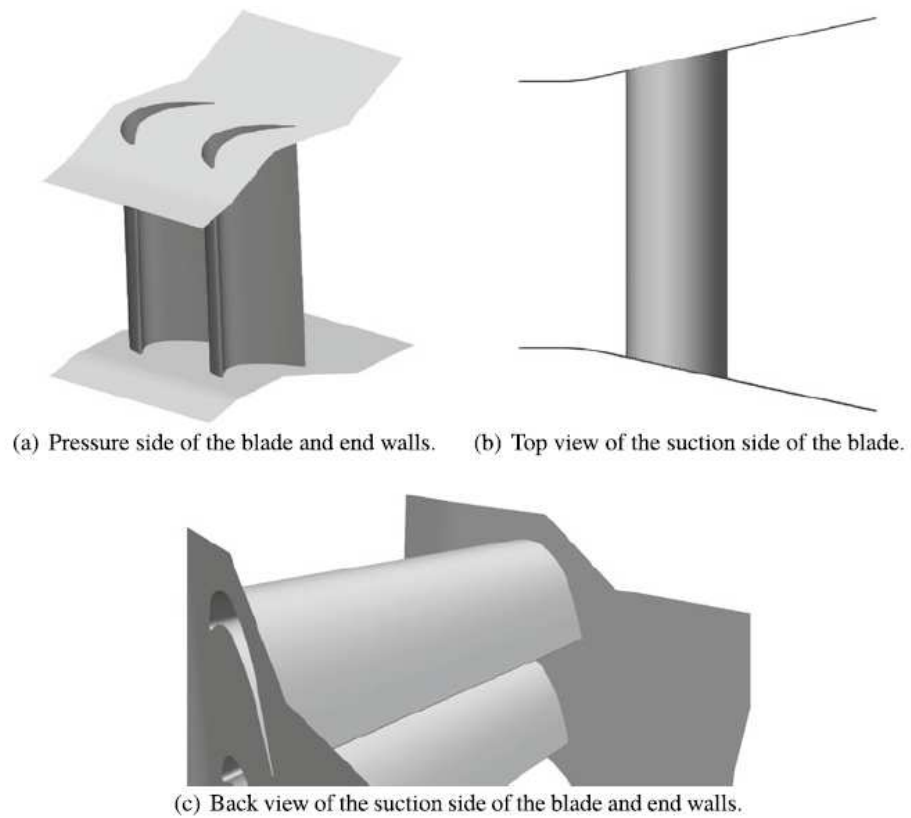
(a) Pressure side of the blade and end walls.   (b) Top view of the suction side of the blade.

(c) Back view of the suction side of the blade and end walls.

Figure 3.1.: Illustration of the MTU-T161 geometry (picture taken from [37])
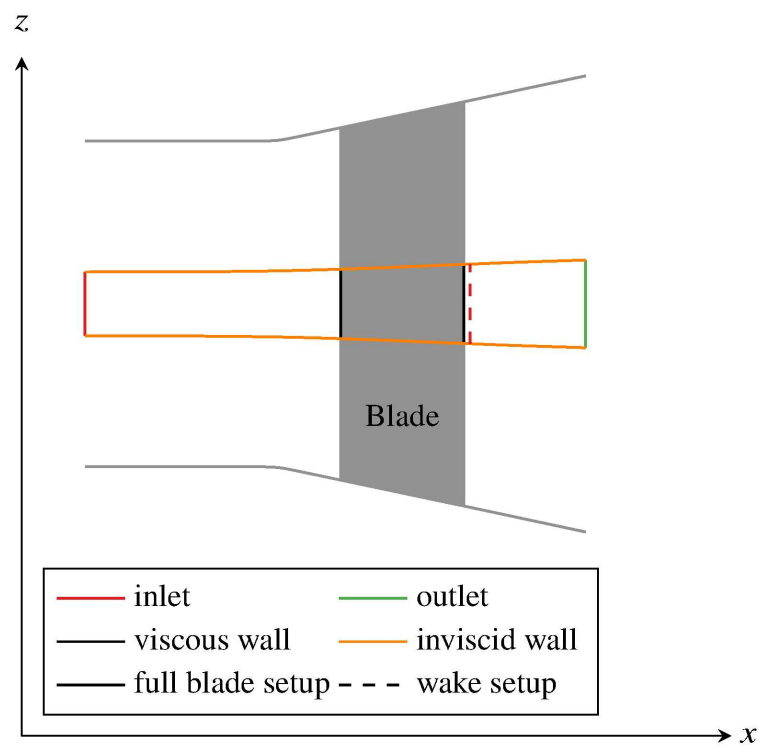

Figure 3.2.: Illustration of the utilized MTU-T161 computational domain

3.2. RANS Simulations Setup

3.2.1. Full Blade Setup Re = 90 000

Here, the entire blade setup for the first operating point is considered. In Tab. 3.1 the boundary conditions values used to setup the case for the current operating point are listed. The grid used for the comparison between the closure models is made up of 27.7×10^6 cells divided in 7 blocks, 2 for the regions respectively upstream and downstream of the blade and 5 for the domain region around the blade. The selection of this grid was based on a comparative analysis with metrics derived from simulations conducted on various meshes. Further details on the grid study procedure can be found in Appendix A. The computational domain is shown in Fig. 3.3.
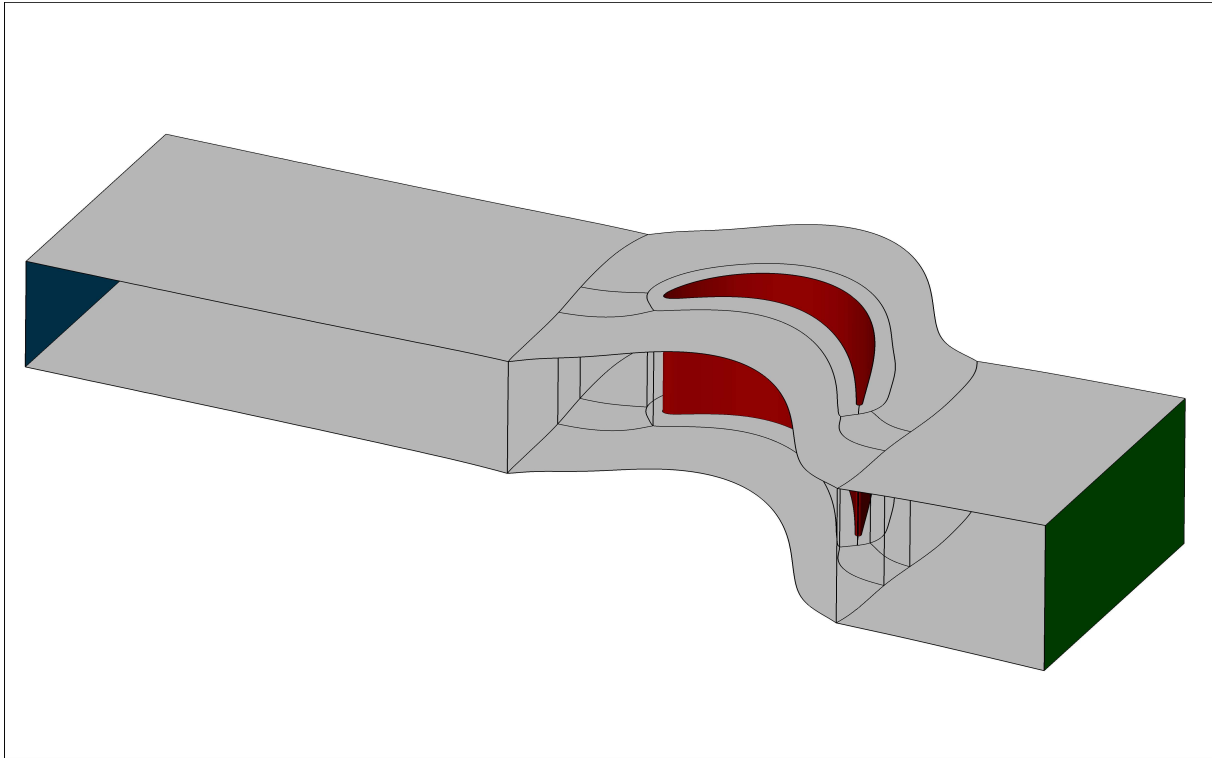

Figure 3.3.: Computational domain for the RANS full blade setup simulations

Table 3.1.: Boundary conditions for the RANS Full blade setup simulations at Re=90 000

Variable	Value
Reynolds Number	90 000
Mach Number	0.6
Turbulence Intensity at L.E.	3.97 %

As said before, in the pitch wise direction periodic boundary conditions are applied; for the various panel groups, the respective boundary conditions are reported in Tab. 3.2. The panels constituting the external parts of the domain have been defined as inviscid

walls, while the blade panel is set as a viscous wall. In Tab. 3.3 the settings used by the flow solver to perform the RANS simulations for the $Re = 90\,000$ operating point are summarized. Further information regarding the the 2009 version of $\gamma - Re_\theta$ transition model, used for the Menter SST 2003 k-ω turbulence model can be found in [36] and [19]. For what concerns the parameters that describe the gas model, assumed to be ideal in throughout the entire work, they are reported in the section 2.1.1 of the previous chapter.

Table 3.2.: Panels boundary conditions and settings for RANS full blade setup simulations

Panel Type	Boundary Condition	Wall Treatment	Heat Transfer
External Walls	Inviscid Wall	-	Adiabatic
Blade	Viscous Wall	Low Reynolds	Adiabatic

Panel Type	Boundary Condition	Method Steady	Average Type
Inlet	Inlet	Steady 2D	Flux Average
Outlet	Outlet	Steady 2D	Flux Average

Table 3.3.: Global settings for the RANS full blade setup simulations

Setting	Menter 2003 SST k-ω	SSG/LRR-ω
Turbulence Treatment	(U)RANS	(U)RANS
Solution Method	ILU	ILU
Stagnation Point Anomally Fix	Kato-Launder	-
Rotational Effects	Off	-
Transition Model	$\gamma - Re_\theta$	$\gamma - Re_\theta$
Transition Model Version	Menter 2009	Menter 2009
Heat Flux Model	Constant Prandtl	Constant Prandtl
Turbulent Prandtl Number	0.9	0.9

Every ran simulation for this setup has converged after around $15\,000$ iterations, with residuals final values below 1×10^{-8}.

3.2.2. Wake Setup Re = 90 000

In this part, the wake setup with its features is analyzed. As suggested by the name, only the region downstream of the blade is considered and so, the computational domain consists of a single block in the shape of a parallelepiped, with slightly diverging sidewalls as shown in Fig. 3.4; this block, on which the simulations were performed is composed of roughly 52.5×10^6 cells. Even for this configuration, the appropriate grid size was determined through a grid independence study, the details of which are provided in Appendix A. Unlike the previously analyzed case, here there are only three different types of boundary conditions, due to the fact that the blade is missing; the boundary conditions are reported in Tab. 3.4.
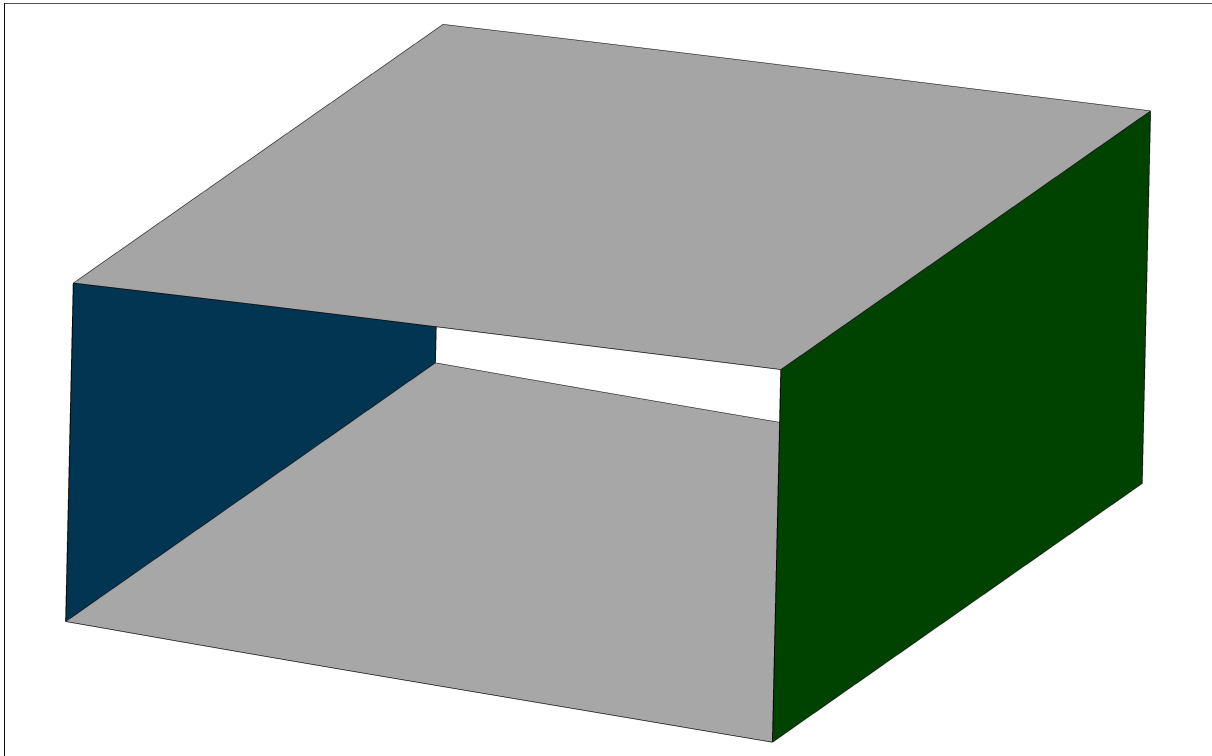

Figure 3.4.: Computational domain for the RANS wake setup simulations

Table 3.4.: Panels boundary conditions and settings for RANS wake setup simulations

Panel Type	Boundary Condition	Wall Treatment	Heat Transfer
External Walls	Inviscid Wall	-	Adiabatic
Panel Type	Boundary Condition	Method Steady	Average Type
Inlet	Inlet	Riemann	Flux Average
Outlet	Outlet	Steady 2D	Flux Average

In addition to the different subdivision into panels groups, there are some significant variations in the boundary conditions regarding the inlet. For this case, in fact, there are no global data (i.e. static pressure) to enter, instead, the whole boundary condition is

specified through an input file which contains all the necessary information. This input file contains the variables required in order to correctly setup the simulations and this is done specifying the different quantities needed by each of the two turbulence models at the inlet plane of the box.
The input file must include the following information:

- Specification of inlet coordinates, which can be made for example through a 2D distribution;

- Specification of inlet flow state, which gives information about the stagnation pressure and temperature of the incoming flow at the inlet. Usually also a value of the static pressure is prescribed for 2D boundary conditions as a fallback for backflow;

- Specification of inlet flow direction;

- Specification of inlet turbulent state, consisting either of turbulence intensity and turbulent length scale or turbulent kinetic energy and dissipation rate for eddy viscosity models. Whereas for Reynolds stress models, there is the additional option to prescribe anisotropic inlet boundary conditions by setting the Reynolds stress tensor or by adding five components of the anisotropy tensor to the isotropic turbulence setup (turbulence intensity and turbulent length scale or turbulent kinetic energy and dissipation rate)

For both models the inlet coordinates are specified using a 2D distribution, with the proper coordinates in the x-, y- and z-direction. The inlet flow state and direction are also specified using the same quantities, i.e the absolute stagnation pressure and temperature and the static pressure (respectively with [Pa] and [K] as measurement unit) for the former and the angles between y- and x-components and z- and x-components of velocity vector for the latter. The only major difference lies in the choice of the variables combination needed to define the inlet turbulence state; in particular for the Menter SST k-ω model, being an eddy viscosity model, the used combination consists of the specific turbulent kinetic energy (in $[m^2/s^2]$) and the specific turbulent dissipation rate (in $[1/s]$). However, for the SSG/LRR-ω method, since it is part of Reynolds stress models, the used variables are the six components of the Reynolds stress tensor $\boldsymbol{\tau^R}$ (only six because the tensor is symmetric) together with the specific turbulent dissipation rate. Regarding this last mentioned quantity, it should be noted that for RANS simulations it is only used to reproduce the TKE field and has no physical meaning by itself while for LES simulation it has a different meaning. To compute these crucial variables, as they can not be directly taken from the LES simulation, the so called "Frozen Approach" method [33] was used. The idea behind this method is to use the complete time averaged LES flow field and only solve the transport equation for the turbulent dissipation rate. This is done thanks to a "frozen simulation", in which proper values of turbulent length scale and turbulent intensity, derived from the LES simulation using a linearized k-ω model, have been prescribed. Finally, performing a cut on the full blade setup frozen simulation (the exact position is located at 6 % of the axial chord length after the T.E. edge of the blade), the boundary conditions for the wake setup can be obtained.

With respect to the settings for the simulation run, a really similar setup to the one for the full blade domain simulations was used.

Every ran simulation for this setup has converged in around 20 000 iterations, with residuals final values below 1×10^{-6}.

3.2.3. Full Blade Setup Re = 200 000

For the simulation of the complete blade configuration at Re=200 000, the utilization of the same grid employed for the lower Reynolds number operating point was validated. This decision was affirmed through a comparison of results with an additional simulation conducted on a more refined mesh. To ensure that the boundary layer was adequately resolved the wall distance was adjusted accordingly. The same settings were applied also for what concerns methods and numerical setup, for both RANS methods; the options used are therefore displayed in Tab. 3.2 and Tab. 3.3. Boundary conditions used for this simulation case are reported in Tab. 3.5.

Table 3.5.: Boundary conditions for the RANS full blade setup simulations at Re=200 000

Variable	Value
Reynolds Number	200 000
Mach Number	0.6
Turbulence Intensity at L.E.	4.09 %

Every ran simulation for this setup has converged in around 15 000 iterations, with final residuals values below 1×10^{-7}.

3.3. LES Simulations Setup

The importance of LES simulations in this research cannot be overstated; as seen before they are used to derive suitable boundary conditions for the wake setup and in addition to that, they can provide a valuable benchmark for evaluating RANS simulations results.

Regarding the utilized LES simulations, they were carried out for both operating points, with the assistance of TRACE software, at IST, in the context of a previous research project [12]. With respect to the numerical setup, to model the subgrid-stresses, the subgrid turbulent eddy viscosity, ν_T, is computed according to the WALE model, which has been already described in section 2.3. Moreover, to introduce artificial turbulence into the flow field, use has been made of synthetic turbulence generator or STG; these tools are extremely valuable as they can create artificial turbulent fluctuations that mimic the behavior of real turbulence, which in the end helps to improve the accuracy of the simulation. For this study, STG were implemented according to Shur et al. [39] by Morsbach and Franke

[29] and finally tested by Matha et al. [24]. For additional information on how the STG method is implemented in the flow solver, refer to the user manual [36].

3.4. Methods

In this section, the softwares used for performing the simulations and the meshing process are introduced.

3.4.1. Flow Solver: TRACE

This section briefly describes the most important aspects of TRACE, the program used to perform the above discussed simulations. The CFD code TRACE (Turbomachinery Research Aerodynamic Computational Environment) has been developed at DLR's Institute of Propulsion Technology since the early 1990s, in order to study complex flows in turbomachinery. Within DLR, TRACE is the standard method for the simulation of internal flows. Outside DLR, universities and other research institutes use TRACE for the scientific analysis of turbomachinery flows. In addition, also companies as the cooperating partner for this research, MTU Aero Engines, employ TRACE in industrial design environments for the design and optimization of turbomachinery components.

TRACE is a density based solver for the Navier-Stokes equations (see section 2.1.1) designed specifically for application on turbomachinery. It works best for Mach numbers between 0.1 and 2.5. For the discretization of the above mentioned equations, the finite volume method is used; for RANS spatial and temporal discretizations, second order Fromm [14] and Predictor-Corrector schemes, are respectively employed. To solve the oscillations problem Van Albada Sqr limiter [42] is applied to the spatial discretization scheme. Regarding LES, to solve the filtered compressible Navier-Stokes equations, a second-order accurate, density-based finite volume scheme was used, applying MUSCL reconstruction (Monotonic Upstream Scheme for Conservation Laws) [43]; the time integration was performed using a third-order accurate explicit Runge-Kutta method. Again, as previously reported, the WALE method was employed to compute subgrid stresses.

3.4.2. Mesh Generators: AutoGrid5™ and PyMesh

For the task of generating grids for the studied geometries, two different softwares were used, depending on the kind of setup of which the mesh was required.

Starting from the full blade setup, the used program was AutoGrid5™, part of Numeca meshing solutions; it allows to create multi-block structured meshes for any kind of turbomachinery, from centrifugal compressors over pumps to wind turbines. To obtain

fully automatic or semi-automatic grids with an optimal quality control, AutoGrid5™ takes advantage of the characteristics of turbomachinery configurations by creating blade to blade grids onto surfaces of revolution. The generation follows four main steps:

1. Definition of the geometry, with blade surface description, definition of hub and shroud surfaces of revolution through curves and specification of additional data needed to handle special features such as splitters, meridional or 3D technological effects.

2. Generation of meridional flow paths. These flow paths define the meridional trace of the surfaces of revolution on which the 3D mesh will be built.

3. Generation and control of 2D meshes on spanwise surfaces. This 2D generation enables the user to control the mesh topology, the grid clustering and the mesh orthogonality along the solid walls.

4. Generation of the final 3D mesh. This generation combines the meridional flow paths and the 2D blade to blade meshes to create the mesh on surfaces of revolution. The use of the conformal mapping between the 3D Cartesian space and the 2D blade to blade space ensures conservation of quality in terms of orthogonality and clustering for each axisymmetric surface mesh.

Finally a check on the parameters of the generated mesh is accomplished, to ensure that the grid meets the requirements.

For the other kind of setup, the wake one, a different software named PyMesh was used to generate the grid. As AutoGrid5™, even this second grid generator creates structured multi-block grids for CFD applications, especially in the context of turbomachinery evaluation and optimization. For the current case study, the instructions to create a proper box grid were provided through a Python script and included parameters such as spacing and information related to the cut plane position and geometry from which to start the creation of the grid. The script was then executed by PyMesh to finally obtain the required grids.

Additional information regarding the meshing and the grid independence study process can be found in Appendix A.

4. Analysis of Results

In the following pages, final results of the simulations and their analysis are reported and discussed. The main goal of this chapter and of the entire research is the comparison between RANS and LES simulations of the various cases and this is primarily done through the evaluation of the entropy generation quantities derived in section 2.5. However, prior to engaging in the analysis, it is imperative to conduct an additional study to validate the obtained results; in the next sections, two metrics are used for this purpose, namely, the isentropic Mach number distribution across the blade (Ma_{is}, computed with TRACE POST) and the total pressure loss distribution (ω, determined according to equation A.2) measured at a certain position in the wake of the blade. This assessment facilitates the determination of the reliability of the obtained results and enables preliminary reflections on the comparison between RANS and LES. The study will be conducted by comparing RANS, LES, and experimental results for the first operating point at Re=90 000. For the higher Reynolds number case, Re=200 000, the comparison will involve only RANS and experimental data. LES simulations were performed as part of another research on the same cascade ([12]). Experimental data used throughout this chapter have been provided from another scientific report ([11]).

## 4.1. First Operating point: Re = 90 000

In this section, the analysis is focused on the results achieved for the lower Reynolds number operating point; for this case, data from both LES simulations and experimental tests are utilized for the validation process. For what concern the comparison of data obtained between the two different kind of simulation, both the full setup and wake setup are investigated in terms of entropy loss generation.

### 4.1.1. Validation of Results

In this first part of the section, computational results are compared with experimental data from [12] in terms of blade loading and wake losses. Fig. 4.1a shows the isentropic Mach number (Ma_{is}) normalized distribution at mid-span of the blade, determined by the static pressure around the blade. Focusing first on the leading edge, the simulations results match the experimental one quite well, both on the pressure and suction side. As expected, LES are more precise with respect to RANS results, but the latter are still providing sufficiently accurate data. This trend is generally followed throughout the entire length of the pressure side, with very little difference between the various results. A small separation zone is detected at around $x/c_{ax} = 0.1$ until after $x/c_{ax} = 0.4$; the LES simulation demonstrates a minor tendency to over-predict flow deceleration compared to

experimental data, whereas the two curves representing RANS simulations closely align across the majority of the profile.
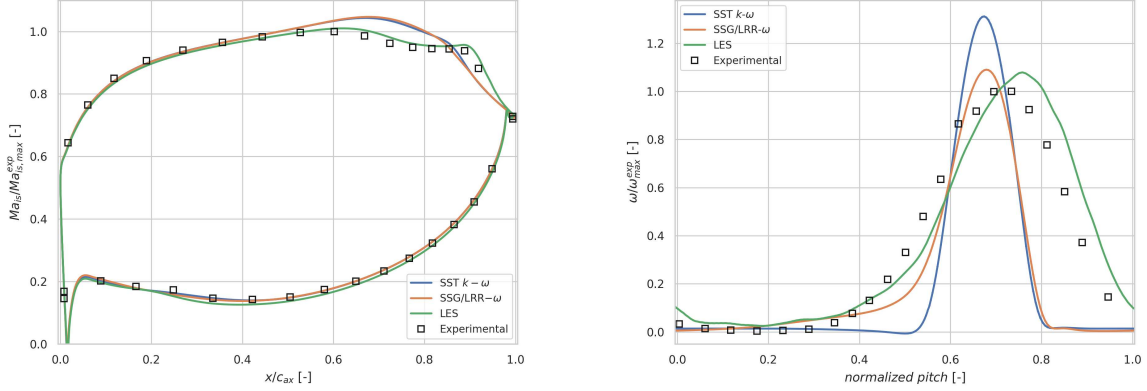
(a) Normalized isentropic Mach number distribution at 50 % of the blade span (full setup)

(b) Normalized wake loss profiles evaluated at 140 % of the axial chord length downstream of T.E. (full setup)
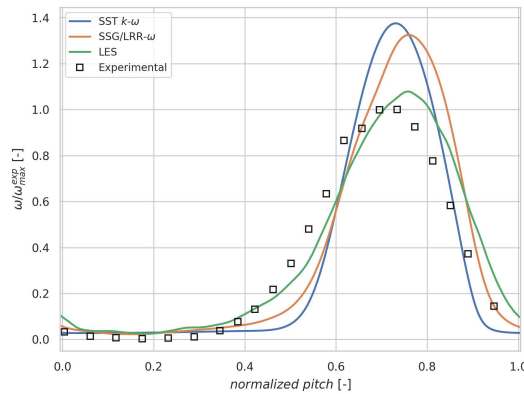
(c) Normalized wake loss profiles evaluated at 140 % of the axial chord length downstream of T.E. (wake setup)

Figure 4.1.: Comparison of averaged quantities for RANS (LEVM and RSM) and LES simulations and experimental data

On the suction side, however, a distinct behavior is observed; while LES simulation can be acknowledged for faithfully replicating experimental tests, the same cannot be asserted for the two RANS simulations. Starting shortly after $x/c_{ax} = 0.3$, the Ma_{is} distributions for both SST k-ω and SSG/LRR-ω models start to divert from the experimental results curve and the gap increases with the Mach number. This results in a different prediction of the Ma_{is} peak value and its position, with LES estimating it at $x/c_{ax} = 0.62$, in good agreement with experiment, while both RANS overestimate the maximum and they place it further downstream, at almost $x/c_{ax} = 0.7$. This leads to an incorrect estimate of the separation, with both SST k-ω and SSG/LRR-ω models failing to replicate the characteristic pressure plateau adequately; in fact, in addition to the initial position also

the final one is incorrectly evaluated, resulting in a shorter separation zone, with the reattachment point located upstream of the actual position. For what concern the LES simulation, the Ma_{is} curve is much more in agreement with the experimental results, especially in the separation zone, with both values and positions estimated fairly correctly. It is interesting to note that, despite SSG/LRR-ω having a separate modelling of stresses, it tends to deliver results comparable to the one obtained with the less complex SST k-ω.

In Fig. 4.1b the normalized wake total pressure loss coefficient ω is shown, computed for the full setup according to equation A.2 at a plane located $x/c_{ax} = 1.4$ downstream of the T.E.. The prediction of the separation bubble highly affects the prediction of the wake and it can be easily noticed how both RANS simulations fail to estimate the wake profile correctly, both in terms of peak value and especially with respect to its shape; even the pitch position at which the coefficient reaches its maximum is not properly estimated, with both models predicting an offset for the turning angle with respect to experimental data. More specifically, the SSG/LRR-ω model manages to deliver slightly better results concerning both maximum value and width compared to SST k-ω, but still, the computed wake is substantially thinner than the measured one. This result is in agreement with other studies previously performed under similar conditions [30] where it was correlated to an overestimate of shear stresses and an underestimate of TKE, especially in laminar boundary layers, due to the transition model preventing it upstream of the bubble. Considering instead the LES, it can be seen that there are some differences even here, not regarding the width of the wake which is generally in agreement with the experimental one, but with respect to its position; in fact, starting from $pitch = 0.4$ the curve has an offset in the pitch direction in comparison with the experimental one.

In Fig. 4.1c, the wake loss profile is once again presented, specifically for the wake setup; although the two RANS simulations exhibit higher peak values compared to the previously analyzed configuration, it is readily apparent that the overall shape of both curves closely resembles the behavior observed in the experimental data. There is also a slight improvement in estimating the maximum position of the curve. The attainment of this outcome is attributed to the utilization of boundary conditions derived from temporally mediated LES data, allowing the simulations to specifically focuses on reproducing the mixing process within the wake.

Hence, it can be asserted that both RANS simulations encounter challenges in accurately reproducing the fluid behaviour within both the separation zone and the wake; this is most likely due to inadequate resolution of turbulent structures. Similar conclusion were also gained by other studies as for example [10] and [28]. In this last paper the authors also test a possible solution to obtain better results for SST k-ω model, in the form of reducing the inflow turbulent length scale but while this seems to improve the prediction of blade loading at first sight, it is source of other problems in predicting the flow behaviour close to T.E. where pressure is not recovered, incorrectly indicating an open separation bubble. On the other hand, when considering the wake setup, RANS simulations exhibit significantly improved performance when it comes to predict wake loss profile.

4.1.2. **Full Blade Setup RANS-LES Comparison**

In the subsequent segment of this section, the analysis is focused in comparing the entropy generation quantities derived from both RANS and LES simulations. Following the approach described by [46], the loss increase caused by various terms in Eq. 2.84 and 2.85 is quantified performing volume integrals of the mentioned quantities, along the whole domain. The terms under consideration can be categorized into three distinct groups. The first group comprises V_M and A_M, representing the influence of mean flow effects. The second group, encompassing P_R, A_k, and H_R, characterizes the entropy generation resulting from turbulence fluctuations. Lastly, the third group involves the SGS stress term V_S and the SGS heat flux term H_S, computed exclusively for LES data. For this study, given also the results obtained from Zhao and Sandberg [46], the terms H_R and H_S were not considered, due to their negligible values when compared to other terms and the total entropy loss. Furthermore, in the case of LES outcomes, the SGS stress term V_S was directly incorporated into the broader term V_M.

In Tab. 4.1 and Tab. 4.2, the total entropy generation by different terms and their percentage compared to overall loss is respectively listed for the examined setup. Regarding the overall loss generation, the RSM predicts a value nearly identical to the one estimated by LES, while LEVM only accounts for around half of it when compared with the previously mentioned methods. It is possible to notice, as the most important role for all the different simulations is played by the the turbulence production term P_R; this represents the energy transfer from the mean flow to the turbulent fluctuations. Although it holds the highest percentage contribution, the absolute value of its influence varies significantly across different simulations. In fact, while the SSG/LRR-ω obtained value is in good agreement with the LES one, it is not possible to say the same about the SST k-ω which predicts a much lower value.

Table 4.1.: Values of entropy generation loss terms for RANS and LES simulations of full setup at Re=90 000

| Terms $[JK^{-1}s^{-1}]$	SST k-ω	SSG/LRR-ω	LES
V_M	0.032987	0.034443	0.031248
H_M	0.000001	0.000001	0.000001
P_R	0.370961	0.900880	0.894431
A_k	-0.001733	0.001325	-0.000764
G_s^{TOT}	0.405682	0.933999	0.926444

The behaviour of this term will be further discussed later on. Regarding the mean viscous dissipation term V_M, a similar contribution to the total loss is achieved for all the performed simulations, with its percentage for the SST k-ω being higher due to the lower value of the overall loss generation. It can be seen that the contribution to the overall entropy generation of the two remaining terms, namely mean heat flux H_M and TKE advection A_k, is much less significant; for the former it can be concluded that it is essentially negligible, while the latter still maintains a not trivial value, even if it is small.

Table 4.2.: Percentage values of entropy generation terms with respect to the total loss for RANS and LES simulations of full setup at Re=90 000

Terms $[JK^{-1}s^{-1}]$	SST k-ω	SSG/LRR-ω	LES
V_M/G_s^{TOT}	8.13 %	3.69 %	3.37 %
H_M/G_s^{TOT}	0 %	0 %	0 %
P_R/G_s^{TOT}	91.44 %	96.45 %	96.55 %
$-A_k/G_s^{TOT}$	0.43 %	-0.14 %	0.08 %

To better understand the spatial distribution of entropy generation mechanisms, its evolution for the various terms is reported in Fig. 4.2 by integrating over the volume between the inlet and the outlet plane. Focusing first on terms representing mean flow effects, V_M and H_M, it becomes evident that the overall trends of the RANS simulations align well with those observed in the LES curve. The increase of both quantities is distributed across the entire blade surface, and can be attributed to the fact that the generation of mean flow entropy takes place predominantly within the blade boundary layer. This behavior is corroborated by the spatial distribution of turbulence production computed on a plane at the blade mid-span (see Fig. 4.3). Regarding V_M, there is a rapid increase nearby the L.E., which can be explained by high values of the viscous stress tensor components and therefore, by strong velocity gradients in the region. Ultimately, both variables exhibit a nearly constant behavior beyond the trailing edge. Taking a closer look to the chart for P_R, it is possible to better understand the numerical values seen previously. While the SST k-ω and LES simulations curves feature a steady but modest increase across the blade, the SSG/LRR-ω one is characterised by a steep rise from close to the L.E. to the T.E.. This behavior can be attributed to the model's tendency to overestimate Reynolds stresses, especially in the proximity of the stagnation point and within the blade passage. In Fig. 4.4 the contour plot of the turbulence production term (with increasing order of magnitude, from purple to yellow) is reported for the three different simulations, showing a significant difference in intensity for the Reynolds Stress Model. It is also noteworthy to observe that, up to the aft region of blade the suction side where separation occurs, the LEVM exhibits favorable agreement with the LES. However, beyond this point, notably astride the trailing edge, the disparity between the curves widens, with the SST k-ω model ultimately leading to a significantly lower terminal value. This behaviour is evident in the larger area affected by turbulent production in Fig. 4.4c. Ultimately, the fact that the SSG/LRR-ω predicts a final P_R value close to the LES estimated value is due to a lucky cancellation of errors. For what concern TKE advection, it is observed that the LES curve exhibits a sudden negative jump precisely at the inlet: this phenomenon is most likely attributed to losses introduced by synthetic turbulence generator (STG) within boundary conditions. Consequently, this discrepancy results in a vertical offset between this and the RANS related curves. The variable trend is then generally the same for all simulations until the L.E., at which the LEVM starts to deviates from the other simulations, not able to detect the A_k rise, which only begins around the position where separation occurs. While it may seem that the RSM accurately captures the evolution of A_k, a closer examination reveals that again, the anomaly occurring at the blade L.E. significantly influences and contributes to the increase in the variable value. This is caused by the production term in Eq. 2.47 and the presence of strong velocity gradients due to
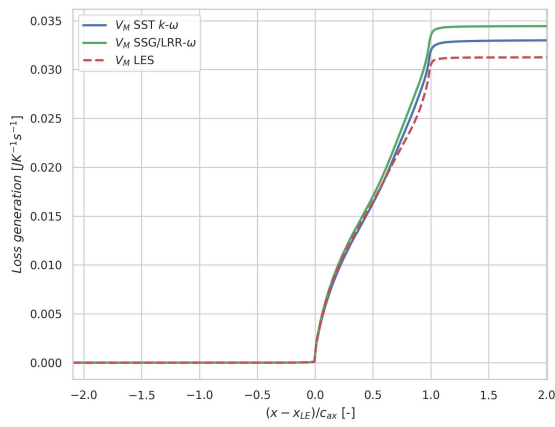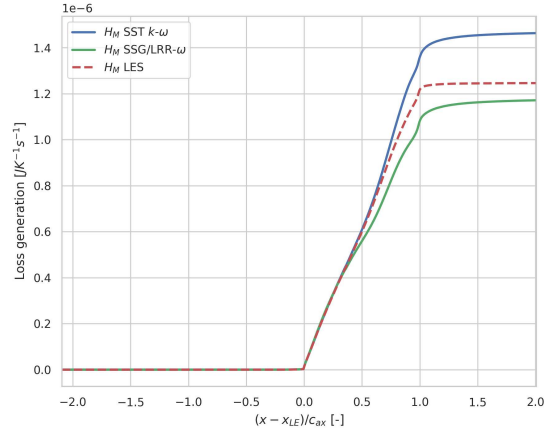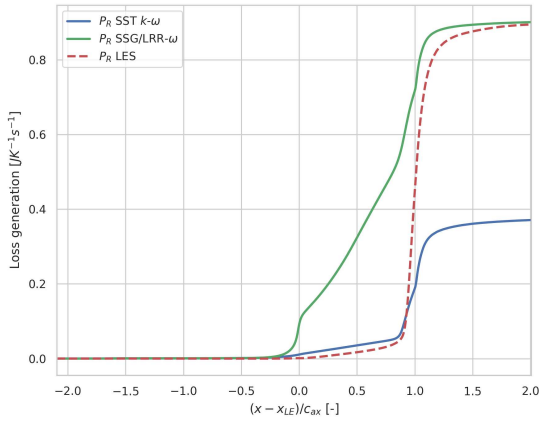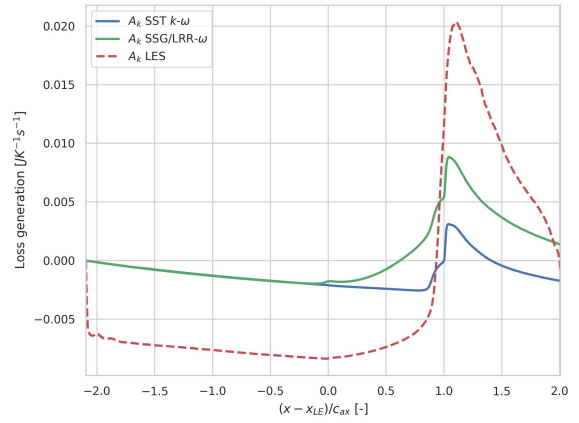
(a) Mean viscous dissipation V_M

(b) Mean viscous heat flux H_M

(c) Turbulence production P_R

(d) Turbulent kinetic energy advection A_k

Figure 4.2.: Comparison of entropy generation term integrals, derived from RANS and LES simulations, for the full blade setup at Re=90 000
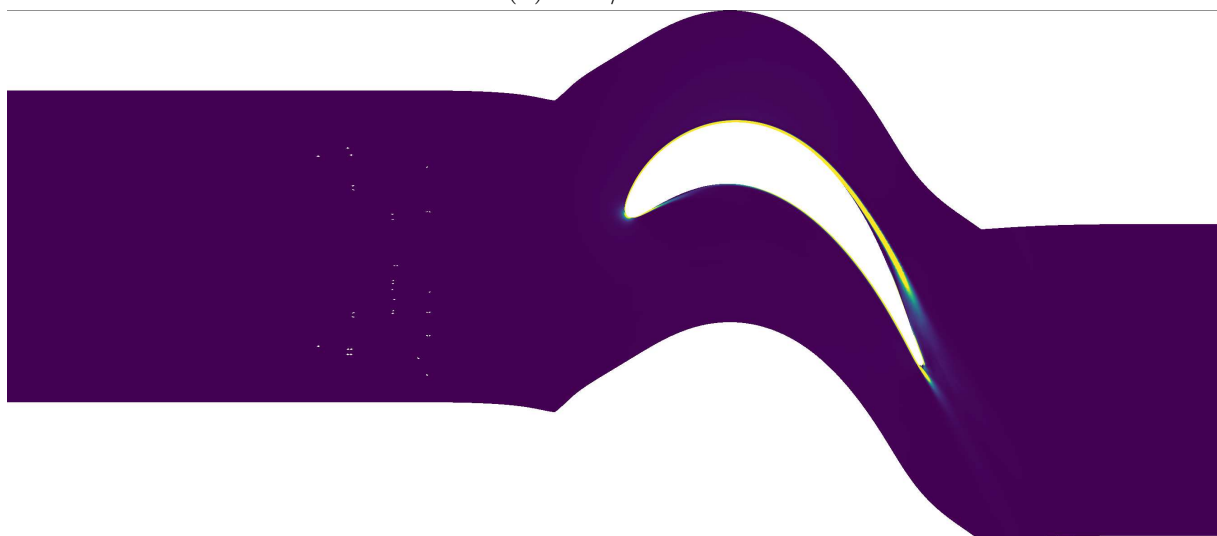
the fluid stagnation. For all simulations, an increase is witnessed in the aft part of the blade reaching the peak slightly after the T.E., even if there is a significant gap between RANS and LES. Further downstream A_k decreases, reaching a negative final value for SST k-ω and LES and slightly positive one for the SSG/LRR-ω.
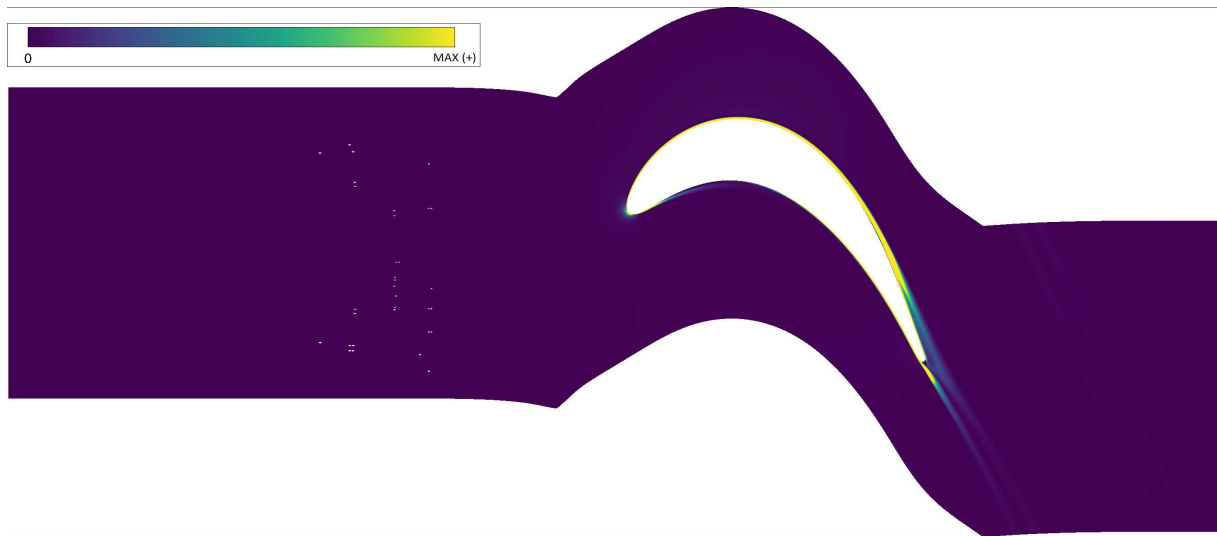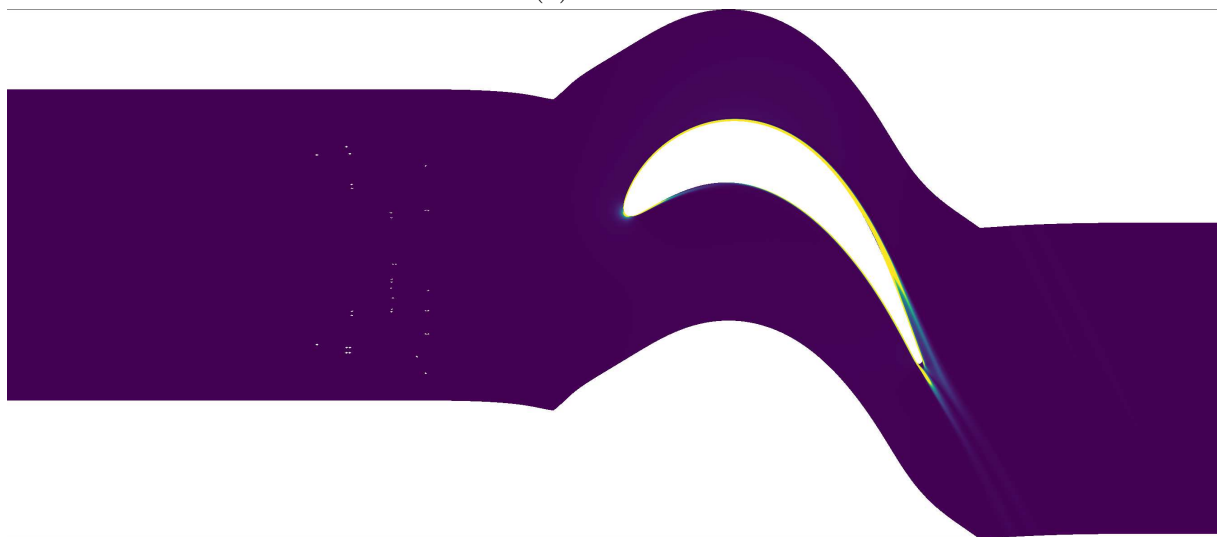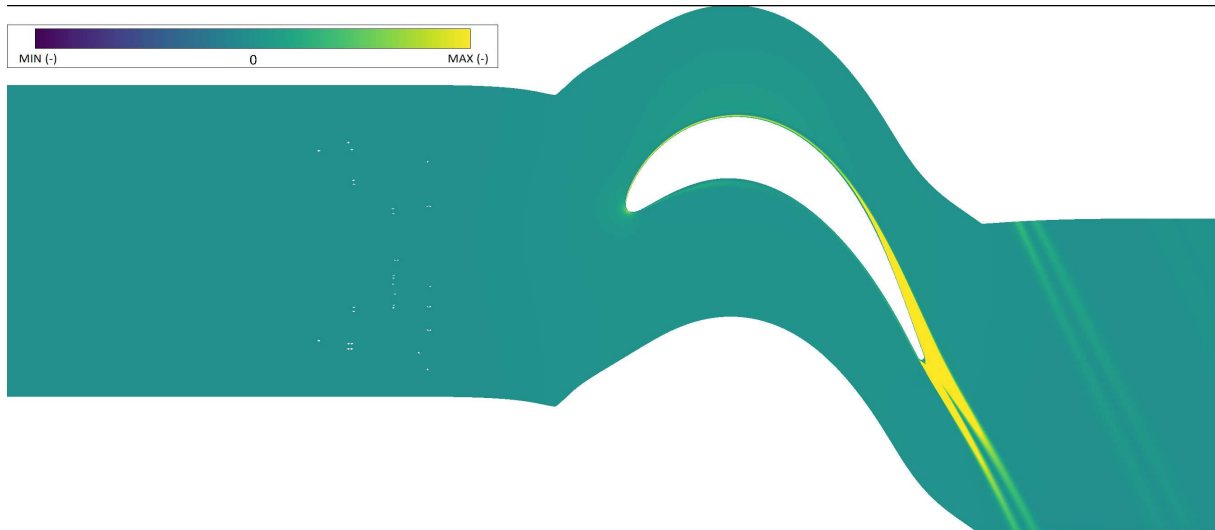
(a) SST k-ω
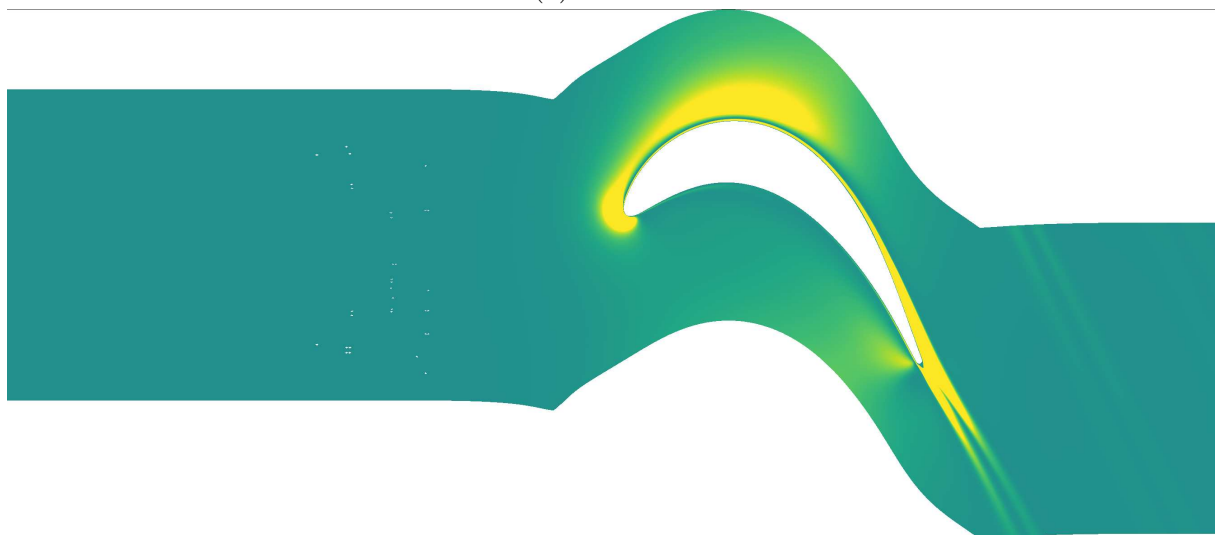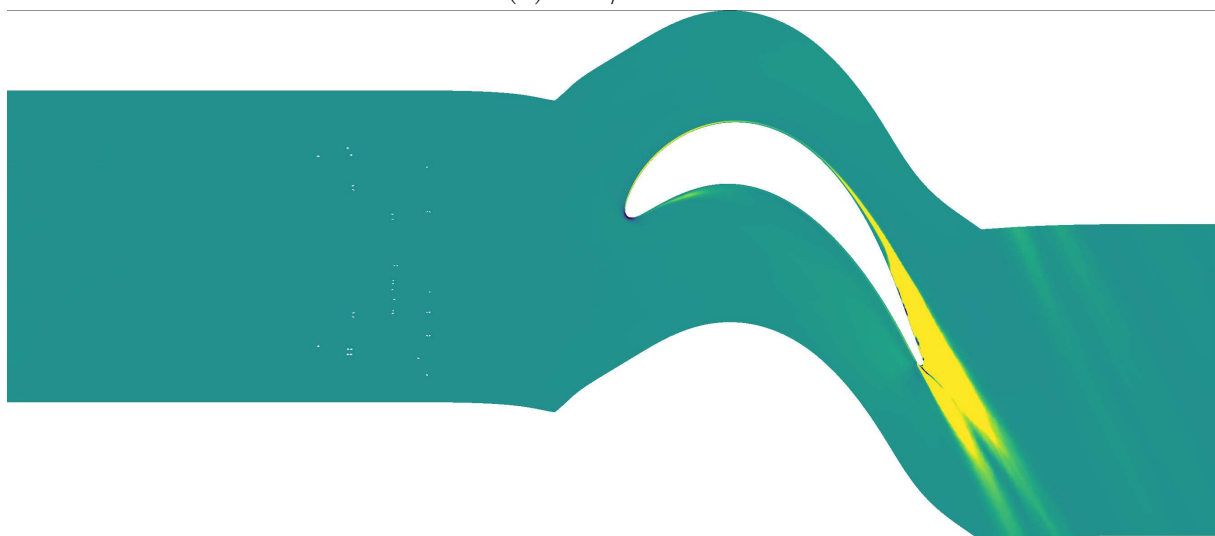

(b) SSG/LRR-ω

(c) LES

Figure 4.3.: Mean viscous dissipation term (V_M) contour plot for each simulation

(a) SST k-ω

(b) SSG/LRR-ω

(c) LES

Figure 4.4.: Turbulence production term (P_R) contour plot for each simulation

4.1.3. Wake Setup RANS-LES Comparison

In this section, the entropy generation analysis is conducted concerning the wake setup, utilizing the same terms as discussed previously. As described in section 3.2.2, the wake setup inlet is located at 106% of the axial chord and so the simulations only perform the wake mixing in the computational domain. For RANS, the flow state at the inlet is described based on quantities derived from time-averaged LES data. It will become evident later on, that this approach significantly impacts the ultimate results.

Tables 4.3 and 4.4 present the overall entropy variation, categorized based on the several contributing mechanisms. Once again, it is evident that the most influential term is P_R, registering values of approximately 90% across all three simulations. However, it is important to highlight a substantial disparity in its absolute value when comparing the three employed methods. Specifically, SSG/LRR-ω predicts a final value closer to that of LES, in contrast to SST k-ω, which is presumably attributed to the superior modeling of Reynolds stresses, facilitated by the availability of a transport equation for estimating these quantities in the former method. The second most conspicuous contribution arises from the TKE advection term, exhibiting a negative final value in both RANS simulations, in agreement with the behaviour predicted by LES. Both estimates provided by RANS methods more closely align with the LES results, compared to the turbulence production term, thanks to a well predicted TKE distribution in the wake region. The two parameters representing mean flow effects, V_M and H_M, experience a significant decrease in both absolute and percentage values. However, this outcome is not surprising, considering that these terms primarily contribute to entropy generation in the blade boundary layer, which is outside the scope of the investigated domain.

Table 4.3.: Values of entropy generation loss terms for RANS and LES simulations of wake setup at Re=90 000

Terms $[JK^{-1}s^{-1}]$	SST k-ω	SSG/LRR-ω	LES
V_M	0.000370	0.000278	0.000163
H_M	0.000000	0.000000	0.000000
P_R	0.311652	0.243536	0.202803
A_k	-0.022634	-0.022096	-0.019651
G_s^{TOT}	0.334656	0.265910	0.222618

Table 4.4.: Percentage values of entropy generation terms with respect to the total loss for RANS and LES simulations of wake setup at Re=90 000

Terms $[JK^{-1}s^{-1}]$	SST k-ω	SSG/LRR-ω	LES
V_M/G_s^{TOT}	0.11%	0.10%	0.07%
H_M/G_s^{TOT}	0%	0%	0%
P_R/G_s^{TOT}	93.13%	91.59%	91.10%
$-A_k/G_s^{TOT}$	6.76%	8.31%	8.83%

(a) Mean viscous dissipation V_M

(b) Mean viscous heat flux H_M

(c) Turbulence production P_R
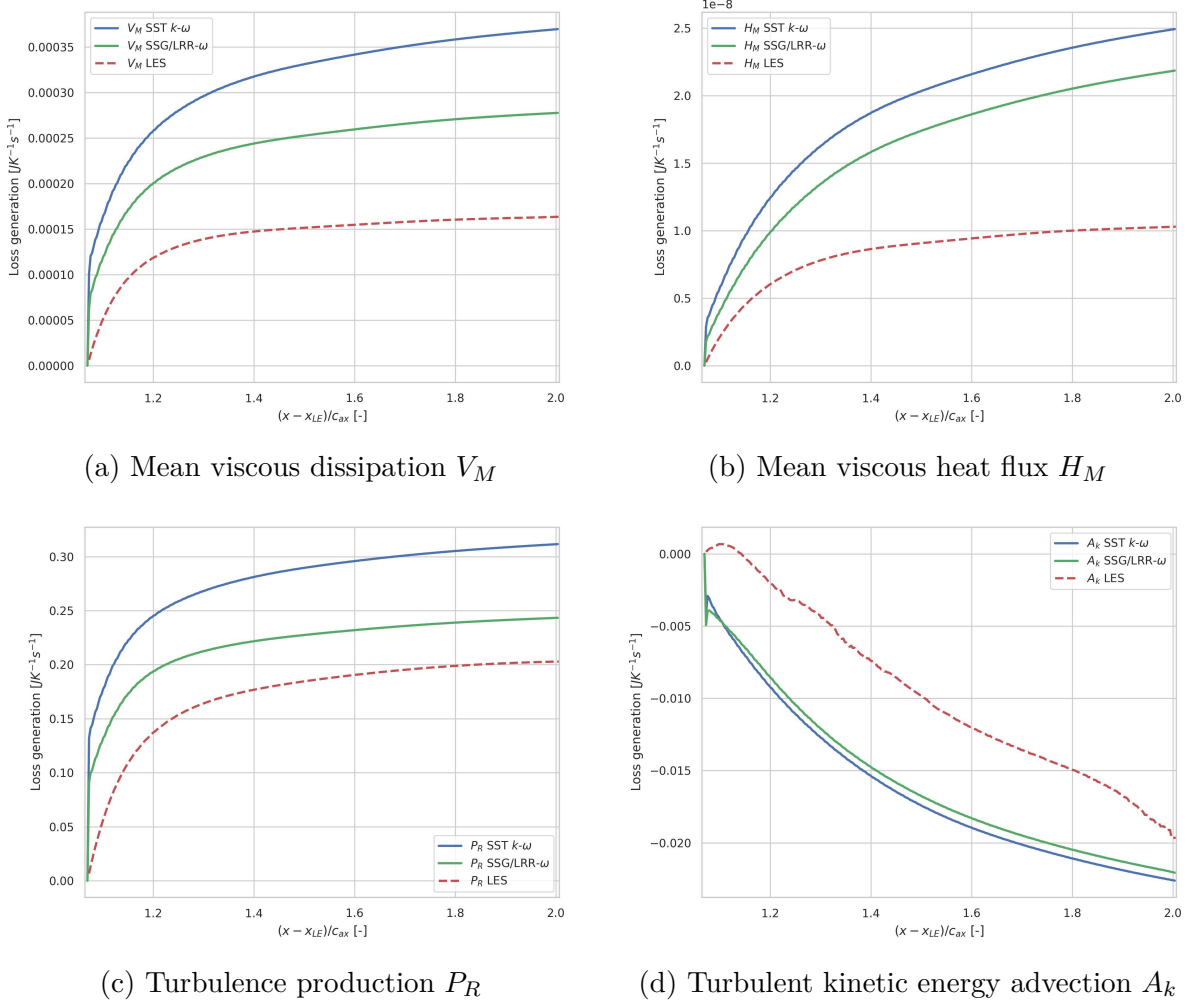

(d) Turbulent kinetic energy advection A_k

Figure 4.5.: Comparison of entropy generation term integrals, derived from RANS and LES simulations, for the wake setup at Re=90 000

Fig. 4.5 illustrates the evolution of the different loss terms for the specified configuration. It is evident that RANS generally aligns with LES for each quantity, demonstrating a good agreement in terms of the overall trend. Regarding the accuracy of RANS simulations, it is observed that the SSG/LRR-ω model globally provides better estimations of the various quantities compared to SST k-ω model. However, the difference between the two is not substantial. In conclusion, it can be asserted that the simulation of the region downstream of the profile significantly benefits from the implementation of boundary conditions derived from Large Eddy Simulation. This is evident in the better level of accuracy that they can achieve when estimating both the values and the evolution of all entropy generation loss terms, compared to results obtained for the entire setup. This behavior can be attributed to the relative ease of predicting the mixing of the wake, despite being a complex mechanism, compared to the challenging prediction of fluid separation occurring in the final region of the blade suction surface.

4.2. Second Operating Point: Re = 200 000

The scope of this section is the analysis of the results achieved for the higher Reynolds number operating point; for this case, data from LES simulations are not available as they were not in good agreement with experimental one and so, only the latter are utilized for the validation process. For the comparison of data acquired through the entropy generation analysis, the full setup is investigated and compared with the results previously obtained for the first operating point.

4.2.1. Validation of Results

In this first part of the section, simulation results derived with the two RANS models are compared to experimental data. The isentropic Mach number distribution, normalized for the peak value of the experimental test is shown in Fig. 4.6a; as for the lower Reynolds number operating point, the simulations match the experiment reasonably well on the pressure side, while again there is a deviation for both models with respect to measurements, on the suction side. In the first part the isentropic Mach is just slightly underestimated by the two simulations until around $x/c_{ax} = 0.3$. Regarding the final portion of the blade, in this case, the region interested by the gap between the curves is smaller with respect to the the previously analyzed point, with the discrepancy starting to be noticeable and increasing after $x/c_{ax} = 0.5$, but not as rapidly as observed before. This pattern persists in yielding an overestimation in both the maximum value and its location. However, it is noteworthy that the calculated values do not exhibit significant deviations from those obtained through experimental means. An area where notable challenges persist, is in identifying the separation bubble formed near the T.E.. As for the other operating point, both turbulence models exhibit a complete inability to capture the plateau, signifying a failure to accurately represent the occurrence of flow separation. In addition to that, it can be noticed that there is also a discrepancy when predicting a correct pressure recovery at T.E., with simulations predicting an higher value for Ma_{is}. Even the normalized wake loss distributions reported in Fig. 4.6b show a similar behaviour to the one already seen for the previous case; in particular, both turbulence models widely overestimate the maximum value of the coefficient and possess a slight offset when predicting the turning angle . Once more, the shape of the experimental curve is not faithfully reproduced, as the simulations yield curves of a slenderer nature. Nonetheless, the discrepancy between simulations and experimental results is smaller when compared with what was shown for the lower Reynolds number operating point. In general, the SSG/LRR-ω model appears to yield superior outcomes, projecting a reduced peak and notably offering a slightly broader loss profile at the curve's base when compared to SST *k*-ω. This model more closely mirrors the characteristics observed in the experimental outline.
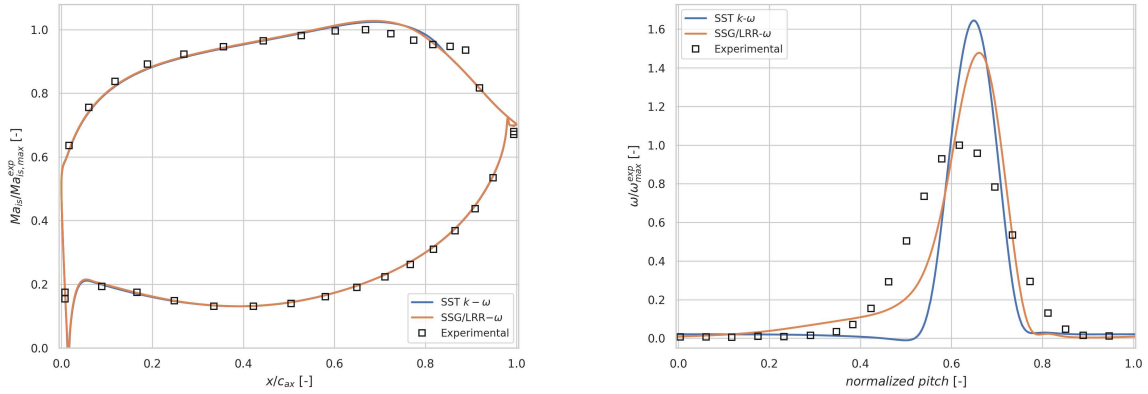
(a) Normalized isentropic Mach number distribution at 50 % of the blade span

(b) Normalized wake loss profiles evaluated at 140 % of the axial chord length downstream of T.E.

Figure 4.6.: Comparison of averaged quantities for RANS (LEVM and RSM) simulations and experimental data

4.2.2. Full Blade Setup: Comparison Between the Two Operating Points

In the followings, the entropy generation loss terms for the higher Reynolds number operating point are examined in terms of absolute values and spatial distribution. Subsequently, these results are compared to the outcomes obtained for the same setup under different conditions. Tables 4.5 and 4.6 present the final values of the variables along with their respective percentages computed as opposed to the total loss generation. Similar to the previous case, turbulence production, P_R, remains the most influential loss term, constituting the majority of losses. Nonetheless, examining both percentage and absolute values, a significant decrease is observed compared to the Re=90 000 case. In fact, focusing on its distribution along the domain, it is seen that the region interested by turbulence production is substantially smaller compared to the previous operating point. In contrast, the opposite trend is evident when comparing the values of V_M, which undergoes a considerable increase. This phenomenon can be attributed to the fact that the mechanism involves the surface of the profile for nearly its entire length.

Table 4.5.: Values of entropy generation loss terms for RANS simulations of entire setup at Re=200 000

| Terms $[JK^{-1}s^{-1}]$	SST k-ω	SSG/LRR-ω
V_M	0.048835	0.053462
H_M	0.000002	0.000002
P_R	0.263205	0.305032
A_k	-0.005784	0.001287
G_s^{TOT}	0.317827	0.357209

Table 4.6.: Percentage values of entropy generation terms with respect to the total loss for RANS simulations of entire setup at Re=200 000

Terms $[JK^{-1}s^{-1}]$	SST k-ω	SSG/LRR-ω
V_M/G_s^{TOT}	15.37 %	14.97 %
H_M/G_s^{TOT}	0 %	0 %
P_R/G_s^{TOT}	82.81 %	85.39 %
$-A_k/G_s^{TOT}$	1.82 %	-0.36 %

For what concern the remaining two quantities, no significant differences are observed.

Finally, Figure 4.7 displays the graphs depicting the evolution of the various loss terms for the two utilized RANS turbulence models at both operating points. The most visually striking difference is observed in the P_R chart (Fig. 4.7c), where it is clear that the SSG/LRR-ω curve for the second operating point, more closely aligns with the SST k-ω curve when compared to those obtained for the lower Reynolds number simulations. Across the blade surface the rise is less abrupt, due to the anomaly discussed in section 4.1.2 being less intense and so causing a less pronounced discrepancy on the results. This explains the notable gap between the final values of the turbulence production term for the two simulations. Examining the evolution of viscous dissipation, as depicted in Figure 4.7a, both models predict a more pronounced increase across the blade surface, ultimately resulting in a higher final value. A similar trend is observed for H_M even though its contribution remains negligible. For what concern TKE advection, the behaviour is consistent between the two simulations until the L.E.. However, beyond that position, similar to what was observed for the previous operating point, the RSM predicts a steep rise across the blade, while the LEVM shows an increase only starting from the separation region. Additionally, the overall loss estimate differs, with SSG/LRR-ω predicting a value very close to the one computed for the other operating point, while SST k-ω delivers a significantly lower value.
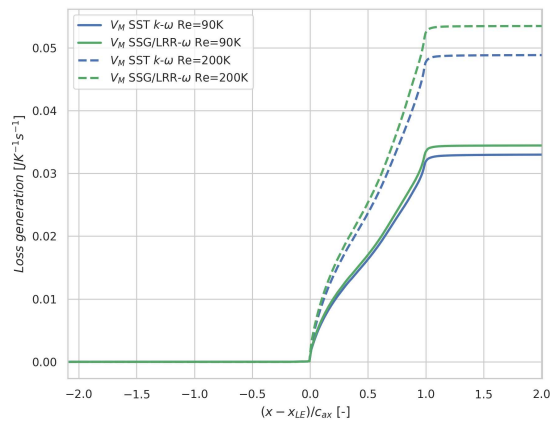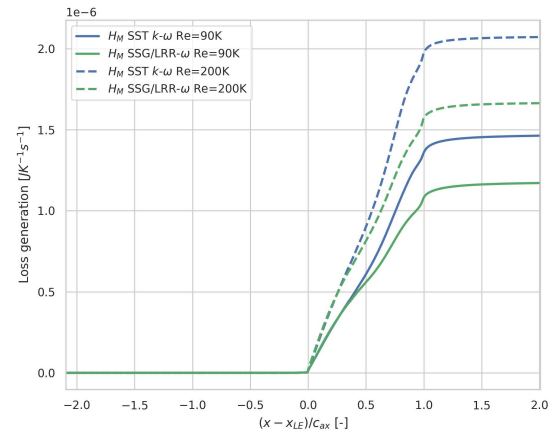
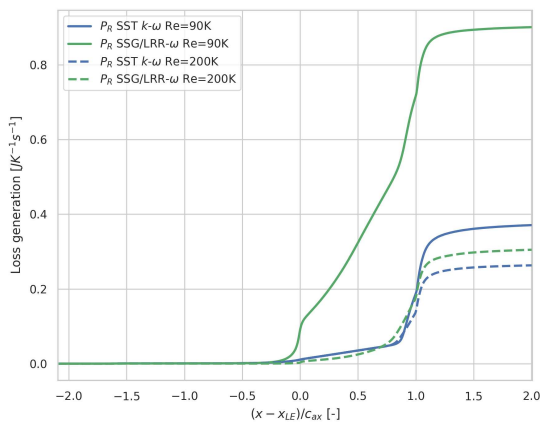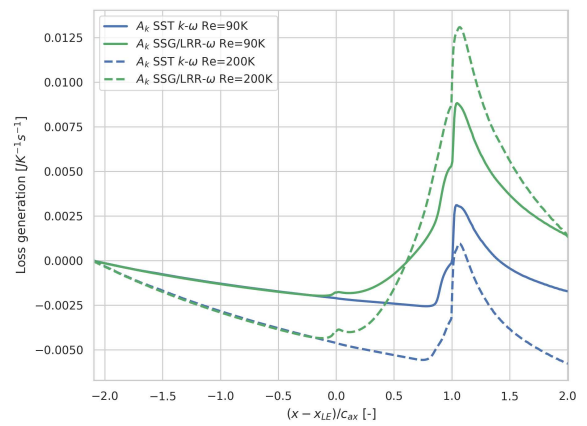(a) Mean viscous dissipation V_M

(b) Mean viscous heat flux H_M

(c) Turbulence production P_R

(d) Turbulent kinetic energy advection A_k

Figure 4.7.: Comparison of entropy generation term integrals, derived from RANS simulations, for the two distinct operating points

5. Conclusion and Future Work

The present study is centered on assessing the performance of Reynolds-Averaged Navier-Stokes (RANS) methods in contrast to Large Eddy Simulation (LES) when simulating the flow around a low-pressure turbine cascade and its mixing in the wake region.

For RANS simulations, two turbulence models with different characteristics were used, namely SST k-ω, belonging to the Linear Eddy-Viscosity Models, and SSG/LRR-ω, part of Reynolds Stress Models family. In order to investigate modeling disparities, multiple simulations were conducted using the TRACE flow solver for two different operating points, each characterized by specific Reynolds numbers, i.e. Re=90 000 and Re=200 000. At the first operating point, two setups were compared: a full blade setup and a wake setup encompassing only the downstream domain. The latter utilized LES-derived inlet boundary conditions. While both setups were analyzed for the initial operating point, the simulations for the higher Reynolds number point were conducted only with the full blade setup. A grid independence study was carried out to determine an appropriate grid resolution that could provide a proper balance between accuracy and simulation stability.

Prior to analyzing the results, a validation procedure was performed for each simulation comparing computed and experimental data for isentropic Mach number distribution over the blade surface and total pressure loss distribution in the wake region. In line with previous research, RANS simulations of the entire setup encountered difficulties in accurately capturing the fluid dynamics within the separation and wake zones at the first operating point. In particular, they were unable to reproduce the characteristic pressure plateau associated with separation and predicted a wake structure thinner than that observed in experiments. Regarding simulations of the wake setup, improved results were obtained with RANS models. While these models tended to overpredict the loss peak value, they accurately reproduced the wake shape observed in experimental studies. These limitations are likely attributed to the inherent inability of RANS models to predict adequately the separation bubble at this specific flow condition. In contrast, LES reached an almost perfect agreement for the isentropic Mach number distribution and exhibited only a slight pitchwise offset in the wake loss profiles. Similar issues were observed at the higher Reynolds number operating point, although the discrepancy between experimental data and RANS simulations was marginally reduced. A comprehensive analysis of entropy loss generation was conducted to evaluate system efficiency. This analysis involved decomposing the overall loss into individual terms associated with various loss mechanisms. For this research the following were considered: mean viscous dissipation, mean heat flux, turbulence production and turbulent kinetic energy advection. Integrating these parameters over the computational domain provided a comprehensive understanding of their individual contribution and spatial distribution to the overall entropy loss generation. While most simulation methods exhibited reasonable accuracy in capturing the overall trends of the various entropy loss terms, the SSG/LRR-ω method exhibited a critical limitation in estimating turbulence production for the entire setup simulation at Re =

90,000. This discrepancy was attributed to an overestimation of Reynolds stresses in the vicinity of the stagnation point and within the blade passage. Conversely, predictions for the wake setup using the SSG/LRR-ω method demonstrated significantly better agreement with LES results both in terms of spatial distribution and overall losses. Across the investigated cases, turbulence production emerged as the most significant contributor to overall entropy generation. This phenomenon primarily occurred in the aft portion of the blade and within the wake region. Conversely, turbulent advection, although similarly distributed throughout the domain, played a considerably less influential role. Regarding the remaining two terms related to mean flow effects, their contributions are observed to be relatively evenly distributed across the entire blade surface due to their confinement within the boundary layer. However, these terms, particularly the mean heat flux, exhibit a comparatively insignificant role in overall entropy generation, with the latter being virtually negligible. As anticipated, the predicted overall losses were marginally lower for the $\mathrm{Re} = 200\,000$ case compared to the $\mathrm{Re} = 90\,000$ case. This observation aligns with expected trends. Notably, turbulence production exhibited a significant decrease, while mean viscous dissipation experienced a moderate increase with increasing Reynolds number. These findings can likely be attributed to the predicted separation region being slightly smaller at the higher Reynolds number.

In conclusion, RANS simulations continue to face significant challenges when applied to flows involving separation and transition. While providing inlet boundary conditions based on LES data demonstrably improved simulation accuracy, this also highlighted the limitations of RANS methods in accurately capturing Reynolds stresses and other turbulent quantities. The SSG/LRR-ω method, except for the already mentioned anomaly, exhibited marginally better performance compared to the SST k-ω, but the complexity of implementation is not necessarily justified by the minimal improvement observed in this specific application.

This study demonstrates that applying the entropy loss generation approach to low-pressure turbines (LPTs) and, by extension, other turbomachines, holds significant potential to yield valuable results and insights on their efficiency. However, both the Linear Eddy Viscosity Model (LEVM) and Reynolds Stress Model (RSM) employed in this investigation exhibited limitations compared to Large Eddy Simulations (LES) in accurately predicting losses. This stems from their inherent inability to capture complex flow phenomena, such as boundary layer transition and separation, with the same level of detail. In this context, potential solutions include refined calibration of existing turbulence models or the development of novel models capable of more accurate predictions of turbulent quantities, such as Reynolds stresses. In recent years, there has been a surge of interest in utilizing machine learning techniques to enhance the predictive capabilities of RANS turbulent models predictions. Finally, as this study focuses on the midspan section, it does not provide insights for RANS model improvement in the critical endwall regions. Therefore, simulations specifically targeting endwall flows would represent a desirable next step to expand the current knowledge and enhance the predictive capabilities of RANS models for LPTs.

A. Grid Independence Study

The purpose of this appendix is to provide the reader with an insight into the grid refinement process carried out as part of this research. To predict the actual phenomena using CFD, a grid design that divides the target space into a finite number of grids is needed first. Given that CFD obtains the approximate solution of the Navier–Stokes equation based on the divided grids, the accuracy of the approximate solution depends on the grid quality. Furthermore, this also has a prominent effect on the accuracy of the entire simulation results because it is affected by the approximate solution of each grid. Therefore, the optimal grid design is indispensable in the improvement of the accuracy of the CFD analysis. Optimal grid designing requires the consideration of the shape type, quality, and number of grids. In particular, the number of grids is a factor that influences the total computational cost and accuracy of simulation analysis results. Coarse grids create a significant spatial discretization error, thereby reducing the accuracy of analysis results. In contrast, too much fine grids may sharply increase the round-off error beyond the truncation error, thereby reducing the accuracy of analysis results. The grid independence test is a process used to find the optimal grid condition that has the smallest number of grids without generating a difference in the numerical results based on the evaluation of various grid conditions. The mesh sensitivity study done for this research follows the guidelines given by this ASME paper [6] and was conducted for both setups considering the Re=90 000 operating point. As described in the paper, first of all it is necessary to define a representative mesh size, h, that for three-dimensional calculations is given by:

$$h = \left[\frac{1}{N} \sum_{i=1}^{N} \left(\Delta V_i \right) \right]^{1/3}, \tag{A.1}$$

in which ΔV_i is the volume of the ith cell and N is the total number of cells used for the computations. Then at least three significantly different sets of grids must be selected to run the simulations and determine the values of a key objective of the simulation study. It is desirable to obtain a grid refinement factor $r = h_{coarse}/h_{fine}$ greater than 1.3, value based on experience. Next steps are aimed at calculating, the apparent order p of the method, the extrapolated values of the chosen variable ϕ_{ext}^{21}, the approximate relative error e_a^{21}, the extrapolated relative error e_{ext}^{21} and in the end the grid convergence index $GCI_{grid-size}^{21}$. For the purpose of this study, the convergence is evaluated in terms of kinetic energy loss, quantified thanks to the related coefficient which has been defined as:

$$\omega = 1 - \frac{1 - (p_2/p_t)^{\gamma - 1/\gamma}}{1 - (p_2/p_{t,1})^{\gamma - 1/\gamma}} \tag{A.2}$$

where p_2 is the outlet static pressure, $p_{t,1}$ is the inlet total pressure and p_t is the total

pressure at the considered location. The total pressure loss coefficient is then evaluated at two different positions of the cut plane, in the wake of the blade, respectively at 140 % and 180 % of the axial chord length.

In the two following sections, data and charts regarding the grid independence study for the two setup at $Re = 90\,000$ are reported.

A.1. Full Blade Setup Grid Study

In Fig. [A.1], the peak values of total pressure loss are reported for the various used grids. It can be seen that the grid are converging with a little difference between the last three grid sizes.
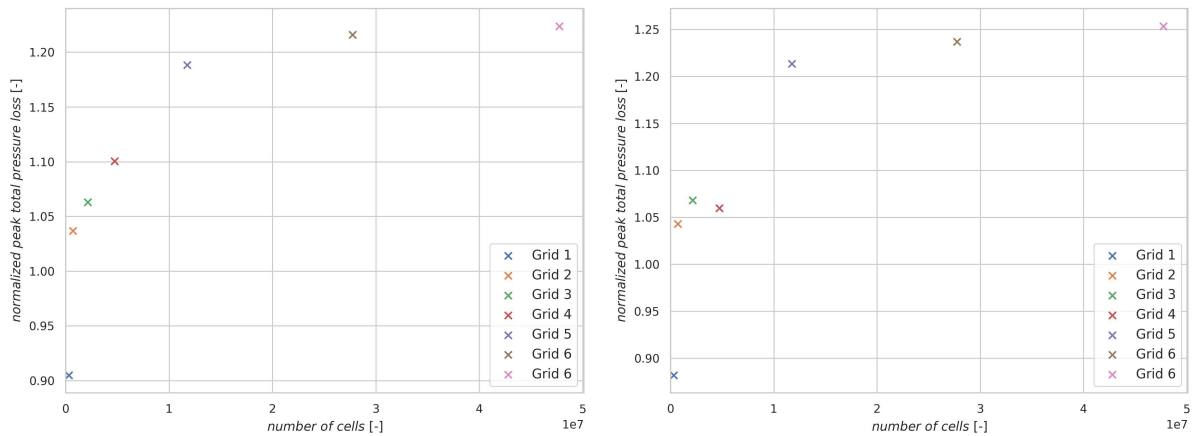
(a) Cut at 140 % of axial chord length.　　　(b) Cut at 180 % of axial chord length.

Figure A.1.: Full blade setup: normalized peak value of total pressure loss in the wake evaluated at the two cut positions.

This trend is confirmed also by Fig. [A.2] and Fig. [A.3] where the total pressure loss coefficient is plotted for every grid over the whole pitch length. It is easy to notice that as the number of grid elements increases, the curves move upwards and tend to get closer and closer until they almost overlap for the last cases. This behavior finally led to choosing "Grid 5" as a reference grid on which to perform the analysis; the use of a mesh with such many elements as the following one is not justified because its increase in accuracy is not significant. If you concentrate on the coarser grids, you will notice an intriguing detail. The line that represents them is not entirely continuous, but there are some minor jumps visible, especially in Fig. [A.2]. The discontinuities are caused by the reduced number of elements that make up the grids in question. As resolution increases, these discontinuities will gradually diminish until they disappear.
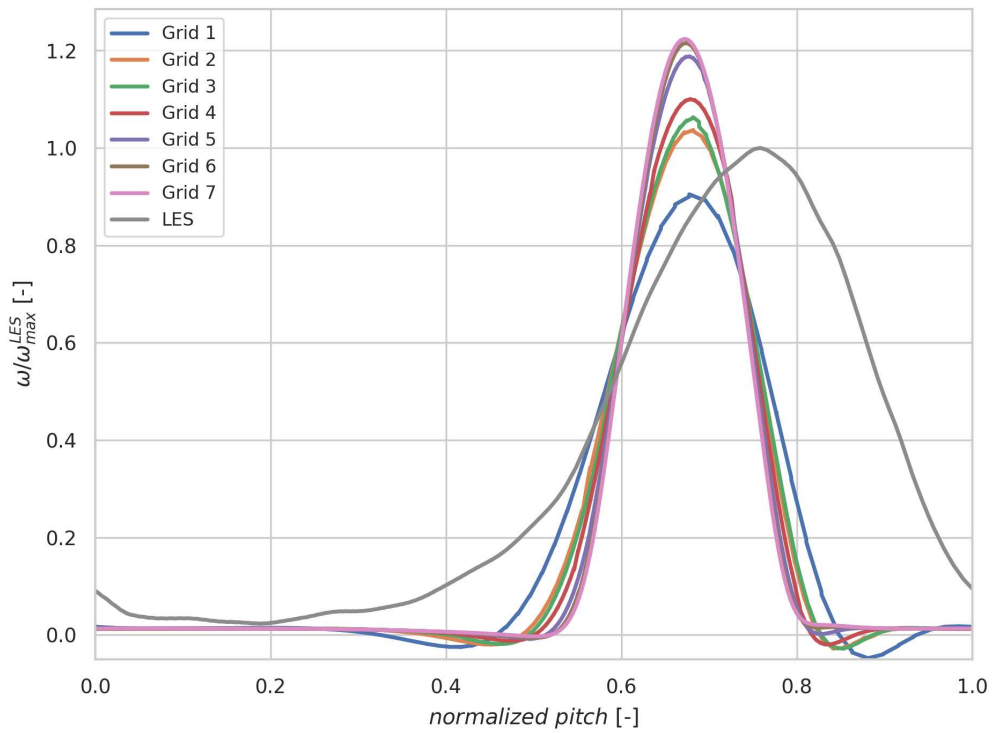
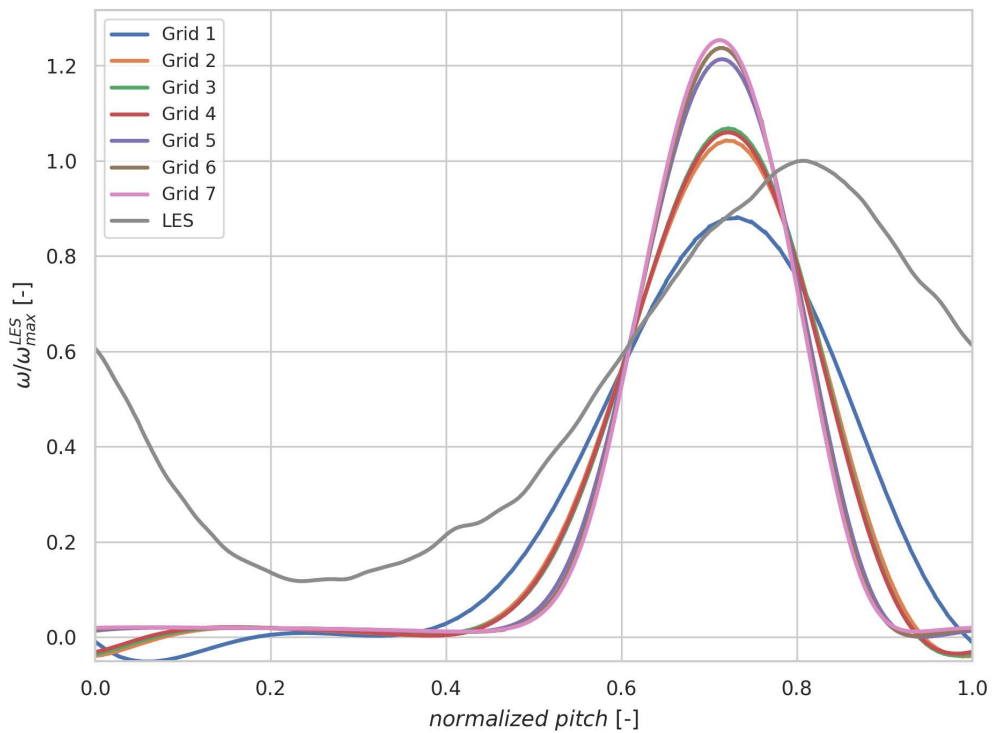Figure A.2.: Full blade setup: normalized total pressure loss in the wake evaluated at 140 % of axial chord length.

Figure A.3.: Full blade setup: normalized total pressure loss in the wake evaluated at 180 % of axial chord length.

A.2. Wake Setup Grid Study

For the wake setup, the iterative process did not converge due to a problem encountered in calculating the order of the method; basically, one of the refinement factor values was too large with respect to the other corresponding one for the use in the q formula (necessary value to compute r) and this resulted in the procedure not converging for the set related to these two values.

(a) Cut at $140\,\%$ of axial chord length.   (b) Cut at $180\,\%$ of axial chord length.
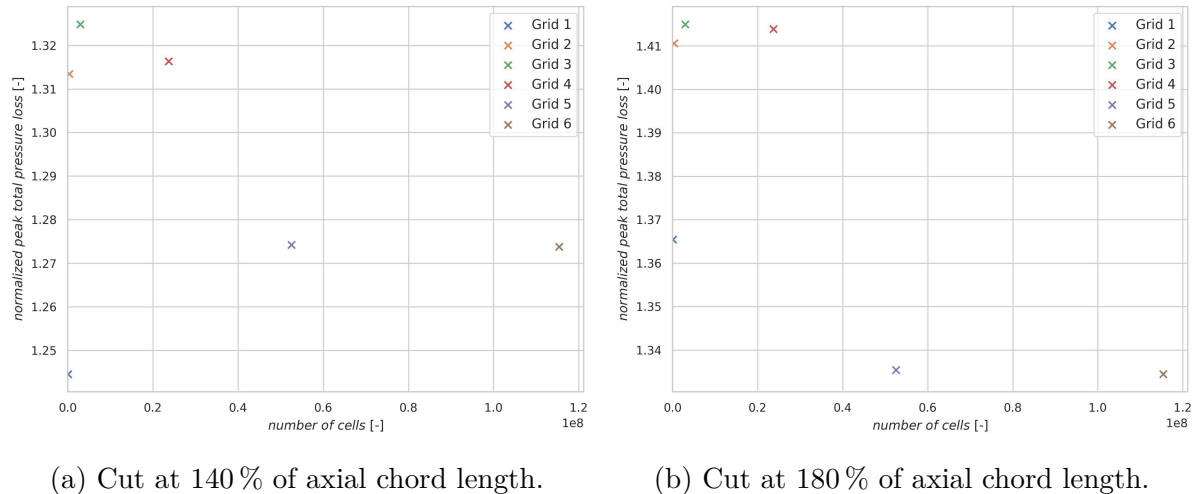
Figure A.4.: Wake setup: normalized peak value of total pressure loss in the wake evaluated at the two cut positions.

Except from this initial problem, it can be seen that even for this setup the study converged, with the last two meshes almost reaching the same peak value of the total pressure loss (Fig. [A.4]). This trend is further confirmed by Fig. [A.5] and Fig. [A.6], where you can see that the two finest grid are practically overlapping. For this reason, as in the previous case, "Grid 5" was chosen for the simulations and analysis of results.
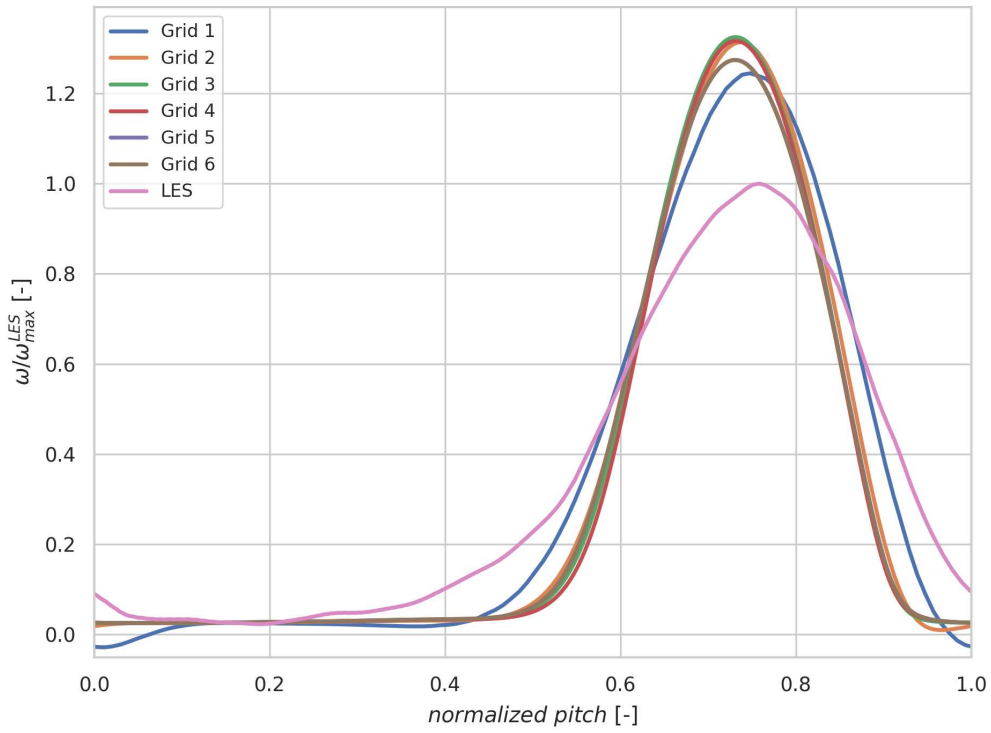
Figure A.5.: Wake setup: normalized total pressure loss in the wake evaluated at 140 % of axial chord length.
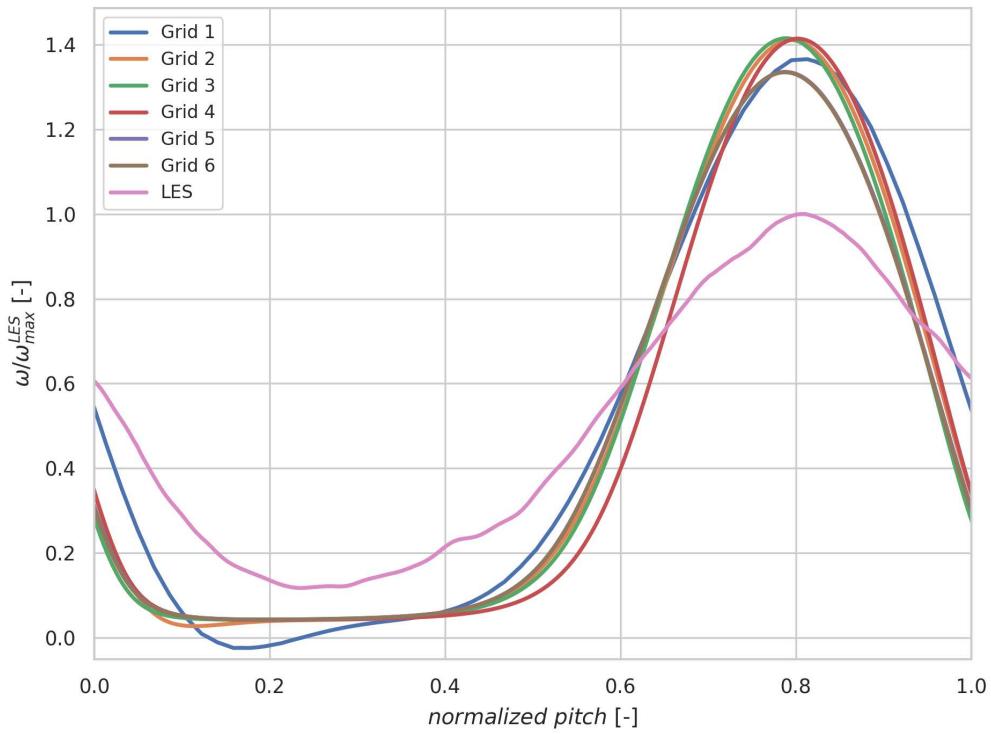

Figure A.6.: Wake setup: normalized total pressure loss in the wake evaluated at 180 % of axial chord length.

Bibliography

[1] BEAR, P. ; WOLFF, M. ; GROSS, A. ; MARKS, C. R. ; SONDERGAARD, R.: Experimental Investigation of Total Pressure Loss Development in a Highly Loaded Low-Pressure Turbine Cascade. In: *Journal of Turbomachinery* 140 (2017), 12, Nr. 3, S. 031003

[2] BEJAN, A.: Second law analysis in heat transfer. In: *Energy* 5 (1980), Nr. 8, S. 720–732

[3] BLOG, Aerospace E.: *Boundary Layer Separation and Pressure Drag.* https://aerospaceengineeringblog.com/boundary-layer-separation-and-pressure-drag/

[4] BOUSSINESQ, J.: *Essai sur la théorie des eaux courantes.* Impr. nationale, 1877

[5] BRADSHAW, P. ; FERRISS, D. H. ; ATWELL, N. P.: Calculation of boundary-layer development using the turbulent energy equation. In: *Journal of Fluid Mechanics* 28 (1967), Nr. 3, S. 593–616

[6] CELIK, I. ; GHIA, U. ; ROACHE, P. J. ; FREITAS, C. ; COLOMAN, H. ; RAAD, P.: Procedure of Estimation and Reporting of Uncertainty Due to Discretization in CFD Applications. In: *J. Fluids Eng.* 130 (2008), 07, S. 078001

[7] DENTON, J. D.: Loss Mechanisms in Turbomachines. In: *Turbo Expo: Power for Land, Sea, and Air* Bd. Volume 2: Combustion and Fuels; Oil and Gas Applications; Cycle Innovations; Heat Transfer; Electric Power; Industrial and Cogeneration; Ceramics; Structures and Dynamics; Controls, Diagnostics and Instrumentation; IGTI Scholar Award, 1993

[8] DENTON, J. D.: Some Limitations of Turbomachinery CFD. In: *Turbo Expo: Power for Land, Sea, and Air* Bd. Volume 7: Turbomachinery, Parts A, B, and C, 2010, S. 735–745

[9] DJENIDI, L. ; ANTONIA, R. A.: Modeling of the Reynolds Stress Transport Equation. In: *AIAA Journal* 35 (1997), Nr. 3, S. 450–455

[10] EISFELD, B. ; RUMSEY, C. ; TOGITI, V.: Verification and Validation of a Second-Moment-Closure Model. In: *AIAA Journal* 54 (2016), 03, S. 1–18

[11] ENTLESBERGER, R.-G. ; MARTINSTETTER, M. ; STAUDACHER, W.: Untersuchungen am Turbinengitter T161 zur Bestimmung der Profildruckverteilung und der Gittercharakteristik. In: *Institutsbericht LRT-WE12-05/02, Universität der Bundeswehr München, Neubiberg, Germany* (2005)

[12] FARD AFSHAR, N. ; KOZULOVIC, D. ; HENNINGER, S. ; DEUTSCH, J. ; BECHLARS, P.: Turbulence anisotropy analysis at the middle section of a highly loaded 3D linear

turbine cascade using Large Eddy Simulation. In: *Journal of the Global Power and Propulsion Society* 7 (2023), S. 71–84

[13] FERZIGER, J. H. ; PERIĆ, M. ; STREET, R. L.: *Computational Methods for Fluid Dynamics*. Springer International Publishing, 2020

[14] FROMM, J. E.: A Method for Reducing Dispersion in Convective Difference Schemes. In: *Journal of Computational Physics* 3 (1968), Oktober, Nr. 2, S. 176–189

[15] GATSKI, T. ; SPEZIALE, C.: On explicit algebraic stress models for complex turbulent flows. In: *Journal of Fluid Mechanics* 254 (1992), 12

[16] GEURTS, B. ; VREMAN, B. ; KUERTEN, H. ; THEOFILIS, V.: LES Modeling Errors in Free and Wall Bounded Compressible Shear Layers. In: RODI, W. (Hrsg.) ; MARTELLI, F. (Hrsg.): *Engineering Turbulence Modelling and Experiments*. Oxford : Elsevier, 1993, S. 325–334

[17] GIER, J. ; HÜBNER, N.: Design and Analysis of a High Stage Loading Five-Stage LP Turbine Rig Employing Improved Transition Modeling. In: *ASME Turbo Expo 2005: Power for Land, Sea, and Air* Bd. Volume 6: Parts A and B, 2005, S. 759–769

[18] GREENSHIELDS, C. ; WELLER, H.: *Notes on Computational Fluid Dynamics: General Principles*. Reading, UK : CFD Direct Ltd, 2022

[19] LANGTRY, R. B. ; MENTER, F.: Correlation-Based Transition Modeling for Unstructured Parallelized Computational Fluid Dynamics Codes. In: *AIAA Journal* 47 (2009), 12

[20] LAUNDER, B. ; REECE, G. ; RODI, W.: Progress in the Development of a Reynolds Stress Turbulence Closure. In: *Journal of Fluid Mechanics* 68 (1975), 04, S. 537 – 566

[21] LENGANI, D. ; SIMONI, D. ; PICHLER, R. ; SANDBERG, R. D. ; MICHELASSI, V. ; BERTINI, F.: Identification and quantification of losses in a LPT cascade by POD applied to LES data. In: *International Journal of Heat and Fluid Flow* 70 (2018), S. 28–40

[22] LENGANI, D. ; SIMONI, D. ; PICHLER, R. ; SANDBERG, R. D. ; MICHELASSI, V. ; BERTINI, F.: On the Identification and Decomposition of the Unsteady Losses in a Turbine Cascade. In: *Journal of Turbomachinery* 141 (2019), 01, Nr. 3, S. 031005

[23] LUDEWIG, T. ; MACK, M. ; NIEHUIS, R. ; FRANKE, M.: Optimization of the blowing ratio for a low pressure turbine cascade with active flow control. In: *9th European Turbomachinery Conference (ETC), Istanbul, Turkey, Mar*, 2011, S. 21–25

[24] MATHA, M. ; MORSBACH, C. ; BERGMANN, M.: A comparison of methods for introducing synthetic turbulence. In: *7th European Conference on Computational Fluid Dynamics*, 2018

[25] MENTER, F. ; KUNTZ, M. ; LANGTRY, R. B.: Ten years of industrial experience with the SST turbulence model. In: *Heat and Mass Transfer* 4 (2003), 01

[26] Menter, F. R.: Two-equation eddy-viscosity turbulence models for engineering applications. In: *AIAA Journal* 32 (1994), Nr. 8, S. 1598–1605

[27] Moore, J. ; Moore, J. G.: Entropy Production Rates From Viscous Flow Calculations: Part I — A Turbulent Boundary Layer Flow. Volume 1: Turbomachinery (1983), 03

[28] Morsbach, C. ; Bergmann, M. ; Tosun, A. ; Kügeler, E. ; Franke, M.: Large Eddy Simulation of a Low Pressure Turbine Cascade with Turbulent End Wall Boundary Layers. In: Marchioli, C. (Hrsg.) ; Salvetti, M. V. (Hrsg.) ; Garcia-Villalba, M. (Hrsg.) ; Schlatter, P. (Hrsg.): *Direct and Large Eddy Simulation XIII.* Cham : Springer Nature Switzerland, 2024, S. 101–107

[29] Morsbach, C. ; Franke, M.: Analysis of a synthetic turbulence generation method for periodic configurations. In: *ERCOFTAC Workshop Direct and Large-Eddy Simulation 11*, 2017

[30] Müller-Schindewolffs, C. ; Baier, R.-D. ; Seume, J. R. ; Herbst, F.: Direct Numerical Simulation Based Analysis of RANS Predictions of a Low-Pressure Turbine Cascade. In: *Journal of Turbomachinery* 139 (2017), 03, Nr. 8, S. 081006

[31] Nicoud, F. ; Ducros, F.: Subgrid-Scale Stress Modelling Based on the Square of the Velocity Gradient Tensor. In: *Flow Turbulence and Combustion* 62 (1999), 09, S. 183–200

[32] Olichevis Halila, G. L.: *A Numerical Study on Transitional Flows by Means of a Correlation-Based Transition Model.*, Instituto Tecnòlogico de Aeronàutica - ITA, Diss., 11 2014

[33] Parneix, S. ; Laurence, D. ; Durbin, P. A.: A Procedure for Using DNS Databases. In: *Journal of Fluids Engineering* 120 (1998), 03, Nr. 1, S. 40–47

[34] Pope, S. B.: *Turbulent Flows.* Cambridge University Press, 2000

[35] Prandtl, L.: 7. Bericht über Untersuchungen zur ausgebildeten Turbulenz. In: *ZAMM - Journal of Applied Mathematics and Mechanics / Zeitschrift für Angewandte Mathematik und Mechanik* 5 (1925), Nr. 2, S. 136–139

[36] Propulsion Technology, DLR's I.: *Trace user guide.* https://www.trace-portal.de/userguide/trace/index.html

[37] *Kapitel* Computational Campaign on the MTU T161 Cascade. In: Rasquin, M. ; Hillewaert, K. ; Colombo, A. ; Bassi, F. ; Massa, F. ; Puri, K. ; Iyer, A. S. ; Abe, Y. ; Witherden, F. D. ; Vermeire, B. C. ; Vincent, P. E.: *TILDA: Towards Industrial LES/DNS in Aeronautics: Paving the Way for Future Accurate CFD - Results of the H2020 Research Project TILDA, Funded by the European Union, 2015 -2018.* Springer International Publishing, 2021, S. 479–518

[38] Schlichting, H.: *Boundary-layer Theory.* McGraw-Hill, 1979 (McGraw-Hill classic textbook reissue series)

[39] Shur, M. L. ; Spalart, P. R. ; Strelets, M. K. et a.: Synthetic Turbulence Generators for RANS-LES Interfaces in Zonal Simulations of Aerodynamic and Aeroacoustic Problems. In: *Flow Turbulence Combust* 93 (2014), S. 63–92

[40] Smagorinsky, J.: General Circulation Experiments with the Primitive Equations: I. the Basic Experiment. In: *Monthly Weather Review* 91 (1963), Nr. 3, S. 99 – 164

[41] Speziale, C. G.: Analytical Methods for the Development of Reynolds-Stress Closures in Turbulence. In: *Annual Review of Fluid Mechanics* 23 (1991), Nr. 1, S. 107–157

[42] van Albada, G. D. ; van Leer, B. ; Roberts, Jr. W.W.: A comparative study of computational methods in cosmic gas dynamics. In: *Astronomy and Astrophysics* 108 (1982), April, Nr. 1, S. 76–84

[43] van Leer, B.: Towards the Ultimate Conservative Difference Scheme V. A Second-order Sequel to Godunov's Method. In: *Journal of Computational Physics* 32 (1979), 07, S. 101–136

[44] Wheeler, A. P. S. ; Sandberg, R. D. ; Sandham, N. D. ; Pichler, R. ; Michelassi, V. ; Laskowski, G.: Direct Numerical Simulations of a High-Pressure Turbine Vane. In: *Journal of Turbomachinery* 138 (2016), 02, Nr. 7, S. 071003

[45] Wilcox, D. C.: *Turbulence Modeling for CFD.* DCW Industries, 2006 (Turbulence Modeling for CFD v. 1)

[46] Zhao, Y. ; Sandberg, R. D.: Using a New Entropy Loss Analysis to Assess the Accuracy of RANS Predictions of an High-Pressure Turbine Vane. In: *Journal of Turbomachinery* 142 (2020), 07, Nr. 8, S. 081008

Acknowledgements

I would like to express my sincere gratitude to my thesis advisor, Engineer Federico Dalla Barba, for his guidance and support throughout my research. I would also like to extend my thanks to the entire staff of the IST at RWTH Aachen, especially Head of Institute Univ.-Prof. Dr.-Ing. Peter Jeschke. My deepest appreciation goes to M.Sc. Johannes Deutsch, my abroad supervisor. His support and encouragement throughout the entire research was fundamental to making sure that I could get this final result, respecting the timing. It's also important to acknowledge that without his help, I probably wouldn't have had the opportunity to make this wonderful experience abroad. Furthermore, I'd like to thank my fellow HiWi Raum colleagues, Alexander and Sebastian, and everyone I met during my stay in Germany. Your presence made the experience even more memorable. Closer to home, I am incredibly grateful to my friends in Padua who have been a constant source of support throughout my studies. I also want to thank all my other friends and family who have endured this journey with me – your unwavering encouragement and belief have been a pillar of strength. Finally, a special thank you to my parents, Federica and Graziano, and my brother Andrea. Their constant encouragement and belief in me have been invaluable throughout this journey.